NASA/TM–1998–206289

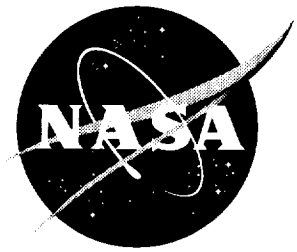

Computational Aeroheating Predictions for X-34

William L. Kleb, William A. Wood, and Peter A. Gnoffo
Langley Research Center, Hampton, Virginia

National Aeronautics and
Space Administration

Langley Research Center
Hampton, Virginia 23681–2199

January 1998

Available from the following:

NASA Center for AeroSpace Information (CASI)
800 Elkridge Landing Road
Linthicum Heights, MD 21090-2934
(301) 621-0390

National Technical Information Service (NTIS)
5285 Port Royal Road
Springfield, VA 22161-2171
(703) 487-4650

Computational Aeroheating Predictions for X-34

William L. Kleb, William A. Wood, and Peter A. Gnoffo
NASA Langley Research Center, Hampton, Virginia 23681

Nomenclature

α Angle of attack, deg

δ_{cs} Control surface deflections, deg (+down)

ϵ Emissivity

ρ Density, slug/ft^3

σ Stefan-Boltzmann constant, $4.76 \times 10^{-13} Btu/ft^2 R^4 - s$

b Wingspan, 27.7 ft

h Altitude, kft

L Overall length, 58.3 ft

M Mach number

p Pressure, lb/ft^2

q Heating rate, Btu/ft^2-s

Re Reynolds Number

T Temperature, °F

V Velocity, ft/s

x Fuselage station, ft

y Buttline station, ft

z Waterline station, ft

Introduction

As early as May 1993, Orbital Sciences Corporation (OSC) of Dulles, Virginia began considering low cost methods to launch relatively small payloads (~1,500 lbs) into space.[1,2] In the fall of 1993, OSC approached NASA to inquire about an alliance which would utilize the Agency's space transportation knowledge base, facilities, and analysis tools. Subsequently, Presidential Decision Directive NSTC-4 led NASA to announce a Cooperative Agreement Notice[3] to build a small reusable launch vehicle (RLV) designated X-34.[1,2,4-6] This was awarded to OSC, teamed with Rockwell International, in the Spring of 1995. By February

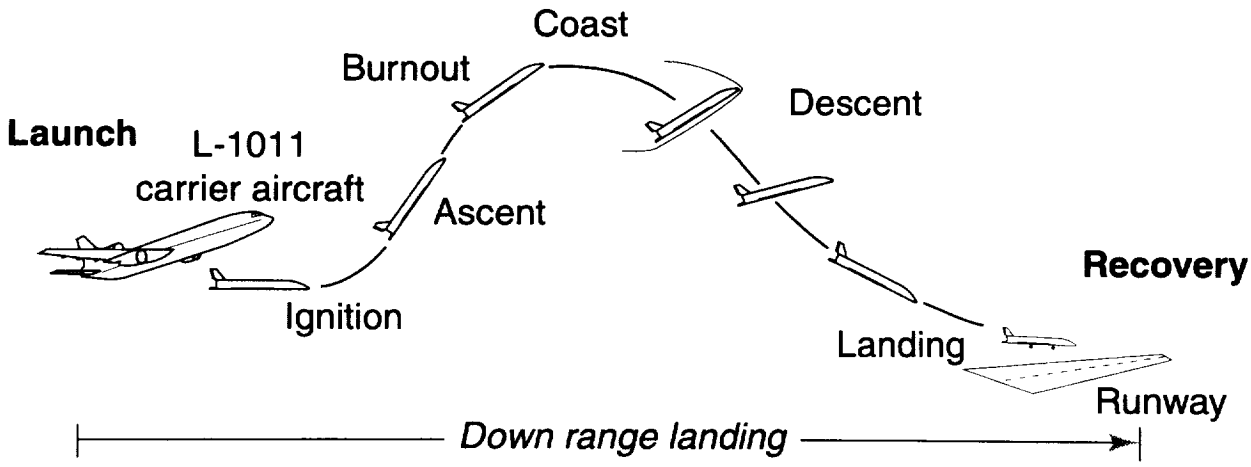

Figure 1. Typical X-34 mission profile.

1996, however, OSC and Rockwell had determined that venture would not be profitable and withdrew from the agreement.[7,8] In the Spring of 1996, NASA solicited proposals for a different vehicle, also designated X-34. OSC was awarded this contract in June of 1996.

The *new* X-34 is to be a suborbital technology demonstrator, capable of flying to Mach 8, reaching an altitude of 250,000 ft, and landing autonomously on a conventional runway. A typical mission profile is shown in Fig. 1. The vehicle is launched from OSC's L-1011, ignites its liquid rocket engine, ascends to altitude, and then coasts to a down-range landing.[a] The vehicle is to serve as a testbed for a multitude of RLV technologies such as composite airframe and propellant tank components, low-cost avionics via the Global Positioning System (GPS), and a flush air data system.[10,11]

This paper presents results used to define and design the Thermal Protection System (TPS) necessary for the vehicle's entry into the Earth's atmosphere. This work is part of a larger effort used to design the TPS, including engineering codes, arc-jet facilities, and wind-tunnel studies.[12–17] The TPS is predominately insulation blankets[17] of the Flexible Reusable Surface Insulation (FRSI) class with SIRCA tiles[16] used only on the leading edges.

NASA Langley's aerothermal contributions consisted of several focused efforts. This paper describes three[b] benchmark-quality, full-vehicle, flight condition computations using state-of-the-art Computational Fluid Dynamics (CFD) to ascertain TPS temperature limits. Riley *et al.*[12] anchored to these two results, expanded the trajectory envelope using a coupled inviscid-boundary layer method. Incorporating the data from this limited array of trajectory points, Wurster *et al*[14] developed a time history of heating rates for the entire trajectory using engineering codes. This analysis yields the heat load for over sixty points on the

[a] A very similar mission profile to the X-15 nearly forty years previous.[9]

[b] An additional case which does not include the aft portion of the vehicle is also presented.

vehicle, providing data necessary to determine the appropriate TPS thickness. In addition to the above, Berry *et al*[13] created an extensive database with several wind tunnel entries, investigating effects of changing Mach number, configuration, angle of attack, Reynolds number, and control surface deflections.

The remainder of this paper begins with a discussion of the numerical tool and geometry employed, and is followed by a brief discussion of the trajectory and the selected points. Next are the results, consisting of: a detailed description of the dominant flow features, a comparison with experiment in the form of surface shear patterns, and surface temperatures, heating rates, and pressures. Finally, a discussion of TPS design issues are discussed, followed by some concluding remarks.

Numerical Method

In the hypersonic continuum regime, the Langley Aerothermodynamic Upwind Relaxation Algorithm (LAURA) CFD tool[18,19] is used to describe the aerothermodynamics of X-34. LAURA is an upwind-biased, point-implicit relaxation algorithm for obtaining the numerical solution to the Reynolds-averaged Navier-Stokes equations for three-dimensional viscous hypersonic flows in thermo-chemical nonequilibrium.[20] The upwind-biased inviscid flux is constructed using Roe's flux-difference-splitting[21] and Harten's entropy fix[22] with second-order corrections based on Yee's symmetric total-variation-diminishing scheme.[23] This is the same computational tool that has been used to describe the aerothermodynamics of blunt body shapes such as Mars Pathfinder,[24,25] Mars Microprobe,[26] Stardust,[27] and COMET;[28] and other vehicles such as X-33,[29] HL-20,[30] Space Shuttle,[31–33] and Reentry-F.[34]

For all of the results contained within, the LAURA code was run assuming air to behave as a perfect gas and the full Navier-Stokes equations were slightly simplified via the thin-layer assumption (see Ref. 35 for rationale). Furthermore, for nearly all the results presented, the flow was assumed to be fully turbulent, using the Balwin-Lomax algebraic turbulence model[35,c] modified with a damping term according to Gupta *et al*[36] as implemented by Cheatwood.[37] However, selected laminar results are also presented to bound the problem.

The wall-temperature boundary condition is specified as the radiation-equilibrium, wall temperature according to the Stefan-Boltzmann relation,

$$q = \sigma \epsilon T^4. \tag{1}$$

The radiative-equilibrium wall temperature, T, is coupled during the solution procedure with

[c]A higher-order turbulence model (*e.g.*, Spalart-Allmaras or κ-ω) which may be more appropriate for the massively separated flow on the lee side of the vehicle, was not available in LAURA at the time of this study.

the wall heating rate, q, where ϵ is the surface emissivity[d] and σ is the Stefen-Boltzmann constant.

This coupled solution procedure between wall temperature and wall heating rate yields accurate temperature and heating rates because of the good insulation features of the selected TPS blankets.

Geometry

The X-34 geometrical description used in this study is designated X0001215 as received from OSC in Initial Graphics Exchange Specification (IGES) format. Figure 2 shows the X-34 geometry as modeled. Overall, the vehicle is similar to the Space Shuttle, having a cranked delta wing planform and vertical tail. Note, however, that the fuselage transitions to rectangular cross section approximately midway back and that the wing terminates before reaching the aft end of the vehicle. The vehicle is to weigh 45,000 lbs with full fuel and have a wingspan, b, of 27.7 ft and an overall length, L, of 58.3 ft.

The coordinate axes are defined in the typical body-oriented manner: x running longitudinally, y along the starboard wing, and z defined by the right-hand rule, pointing upward with the origin located at the nose.[e]

Small modifications were made to the original geometry to allow more tractable grid generation and facilitate obtaining the CFD solutions. These modifications consisted of the following:

- Backward or forward facing steps created by TPS material interfaces such as that caused by the wing leading edge SIRCA tiles and the trailing AFRSI blankets were not preserved as sharp steps. The surface grid lines were mapped onto the stepped surface, but no attempt was made to align them with the discontinuities. As a result, the sharp steps are replaced by ramps.

- The span-wise gaps between the elevons and the body and the elevons and the ailerons were filled in as solid surfaces. Any other gaps or surface irregularities have not been modeled. Past experience has shown that when elevons and ailerons are slaved to move together as is the case for the hypersonic portion of the X-34's flight profile, that the effects of the gap between them is a highly localized phenomenon as shown by Berry *et al.*[13] However, filling the gap between the body and the elevon has a larger effect because it channels flow onto the aft portion of the vehicle which would normally have passed through to the lee-side wake.

[d]A constant emissivity of 0.8 was used for all surfaces.

[e]OSC uses a different origin location.

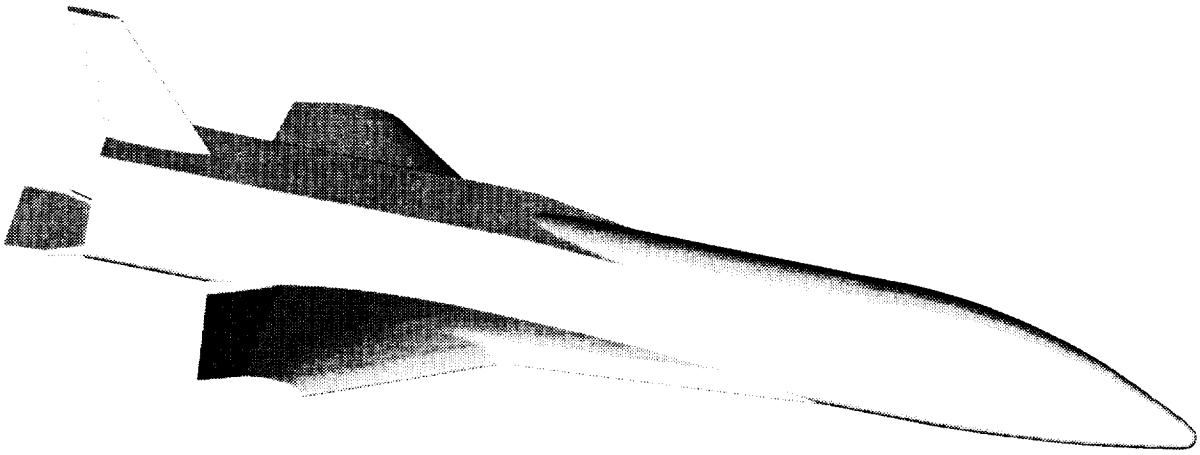

a) Lee side view.

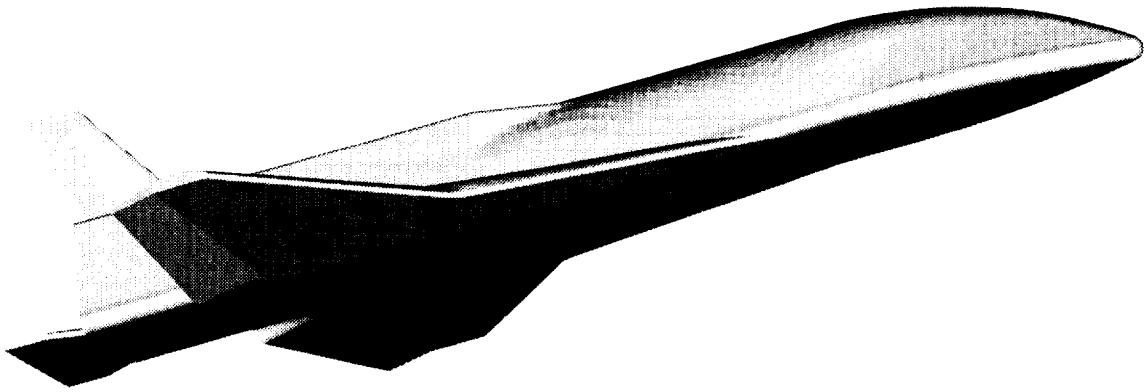

b) Wind side view.

Figure 2. X-34 geometry.

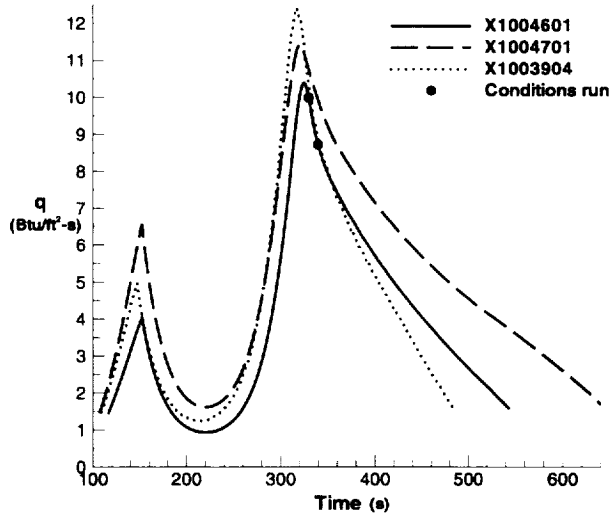

Figure 3. Stagnation-point heating (hot-wall) for three X-34 trajectories.

- The lower, aft portion of the tail surface overhanging the back of the vehicle was clipped off to provide a continuous supersonic outflow boundary condition.
- The vehicle wake and base region including the engine nozzle and lee-side of the body flap were neither modeled nor computed.

The surface and volume meshes were generated using ICEMCFD,[38] GRIDTOOL,[39] GRIDGEN,[40] 3DMAGGS,[41] and VGM[42] as described by Alter.[43] A typical full-vehicle grid including the body flap and wing wake has a total of 70 blocks and 9 million grid points.

Trajectory Cases

Figure 3 shows stagnation-point heating rates, hot-wall, for a 7.11 inch radius sphere[f] as predicted by Fay and Riddell theory for three different X-34 trajectories provided by OSC. The X1004701 trajectory was used by Palmer *et al*[15] and Milos *et al*[16] to predict the heating environment to be encountered by the nose cap and wing leading edge SIRCA tiles. The X1004601 trajectory was used as the reference heating trajectory for the overall TPS design per OSC's request. The actual flight trajectory is anticipated to be closer to X1003904.

Table 1 presents the free-stream conditions and control surface deflections for the cases computed.[g] The points shown in the Table are taken from the X1004601 trajectory and correspond to peak nose cap heating and slightly thereafter when the angle of attack is significantly lowered.

[f]The nose radius of the X0001215 configuration.

[g]Note: for Case 2b the solution was not computed aft of the wing trailing edge.

Table 1. Free-stream conditions and control surface deflections.

Case	δ_{cs} (deg)	h (kft)	M_∞ (-)	α (deg)	V_∞ (ft/s)	ρ_∞ (slug/ft^3)	T_∞ ($^\circ F$)	Re_∞ (-)
1a	0	118.4	6.3	23	6490	1.42×10^{-5}	-22	16×10^6
1b	10							
2a	0	112.1	6	15.2	6110	1.89×10^{-5}	-30	21×10^6
2b	10							

Results

First, the dominant flow field features are presented and analyzed to provide a basis for the discussion of the results to follow. Next, a comparison with experimental data of Berry *et al*[13] is given for Case 2 conditions in the form of near-surface streamlines via the oil-flow technique. Surface distributions of temperature are presented next, followed by a sample of the associated heating rates and an example of the effects of a laminar or turbulent boundary layer.

Note: discontinuities in the figures are a result of block-to-block averaging errors when a block-marching solution strategy was used. These errors are aesthetic only, the computational cell-centered values are globally conservative and consistent across block-to-block boundaries.

Dominant Flow-field Features

Figure 4 shows four stream-wise cuts with contours of pressure non-dimensionalized by free-stream, $\bar{p}$, for Case 1b. Figure 4(a) also includes red lines indicating the location of the other three stream-wise cuts and, in blue, the locations of span-wise cuts that will be shown in Figs. 5 and 6.

As shown in Fig. 4(a), the forebody of the vehicle is enveloped in a highly swept bow shock which intersects with the wing-induced shock. As the flow passes the wing tip the outer wing shock sweeps aftward due to the expansion.

Figure 4(b) depicts a stream-wise cut along the fuselage outboard of the centerline. The wind-side bow shock is shown clearly. Also shown are the faint remnants of the shock created by the deflected elevons; and, at the aft end of the vehicle, the embedded shock due to the deflected body flap. The lee-side shock is also apparent, although somewhat smeared due to a highly stretched grid in this region. Toward the front, on the lee-side, a small expansion-recompression is evident due to a TPS transition. This is followed by a rapid expansion over the canopy region. A second, slight compression is also noticeable due to cross flow effects

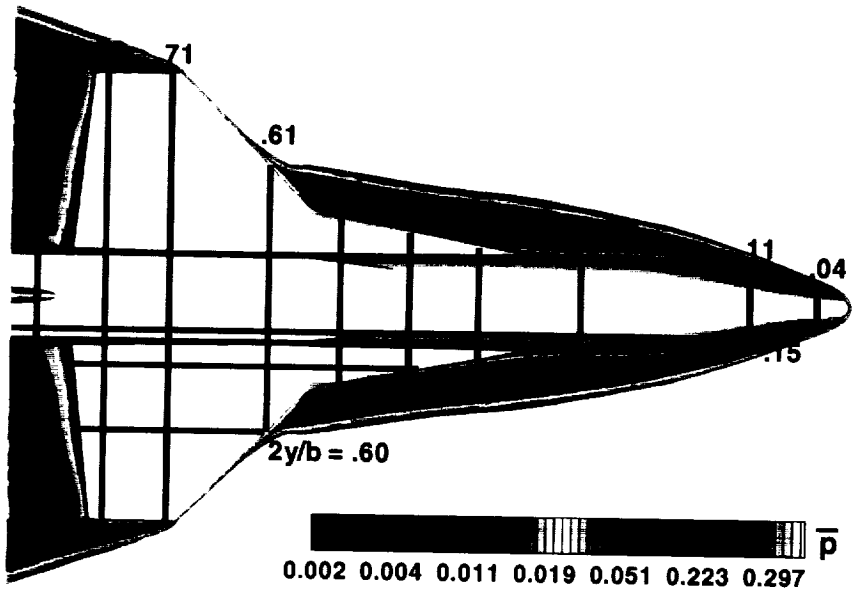

a) In the plane of wing leading edge and nose cap.

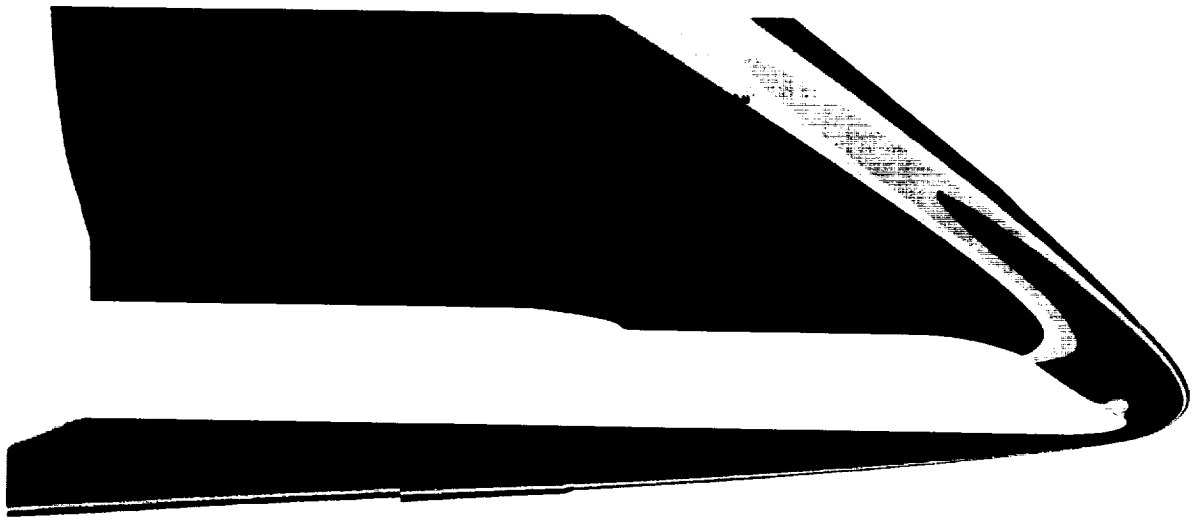

b) Vertically, along fuselage (2y/b=0.15).

Figure 4. Non-dimensional pressure contours for various stream-wise cutting planes (Case 1b).

c) Vertically, along wing and strake (2y/b=0.30).

d) Vertically, along wing (2y/b=0.60).

Figure 4. Concluded.

from the side of the fuselage. This is followed by further expansion, until the point where the fuselage transitions from a rounded cross-sectional shape to one with a considerably smaller corner radius (see Fig. 2(a)). At this juncture, a shock is generated, which is then followed by a small expansion when the transition is complete. The wake of the wing is responsible for the area of lowest pressure just ahead of the tail which again raises the pressure slightly due to an embedded shock.

Figure 4(c) shows a stream-wise cut further away from the centerline, but still well inside of the wing-bow shock interaction. The shock generated by the deflected control surface is readily apparent on the wind side. Another dominant feature present is the wake of the wing and strake which is altered by a fish-tail shock structure emanating from the trailing edge of the wing. Moving outside of the bow-shock interaction area as shown in Fig. 4(d) shows similar features.

Span-wise cuts for Case 1b are shown in Figs. 5 and 6.[h] Figure 5 shows cross-flow streamlines colored by pressure[i] and Fig. 6 shows Mach number contours from 0.2 to 9.0 in increments of 0.2.

The first pair of sub-figures (5(a) and 6(a)) are taken on the forebody, just behind the nose cap. A pair of wind-side vortices is clearly seen near the centerline. There is no evidence of vortices on the lee side at this axial station. The over-expansion and subsequent compression is evident along the side of the fuselage.

A very different picture is evident in Fig. 5(i) which shows a cross-section located near the wing trailing edge. There is no longer any evidence of the wind-side vortices, and a pair of well-defined vortices sit on the lee side of the fuselage. Small wing-tip vortices are present, and the wing-strake vortices lie along the side of the fuselage. The source structure above the wing at mid-span is merely the demarcation of inboard/outboard span-wise flow as well as the location where the flow has either a positive or negative vertical component. Also apparent is a small separation bubble on the inboard wing lee side.

On the wind side the embedded shock due to the deflected control surface is also clearly indicated by a merging of streamlines paralleling the deflected control surfaces. Figure 6(i) also shows the presence of the extensive hour-glass shaped cross-flow shock standing on the fuselage. This shock serves to turn the flow parallel to the vehicle symmetry plane. The vertical gradients in Mach number between the cross-flow shocks (which are not present in pressure – see Fig. 5(i)) are believed to mark the entropy interface between flow that has gone through only the bow shock and that which has gone through both the bow *and* cross-flow shocks.

[h] Recall, the relative vehicle locations are depicted by the blue lines in Fig. 4(a).

[i] No explicit scale is given; as with Fig. 4, blue indicates low pressures while red indicates high pressures.

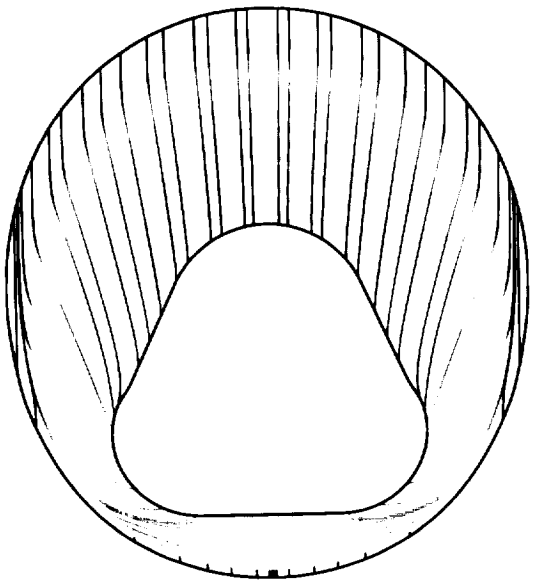

a) Downstream of spherical nose cap (x/L=0.04).

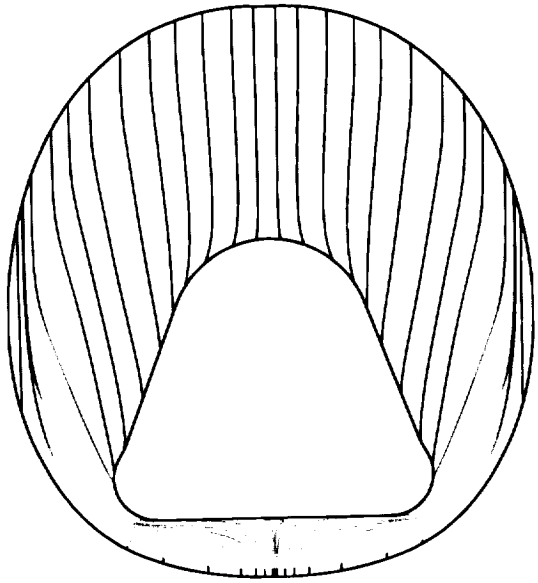

b) Canopy region (x/L=0.11).

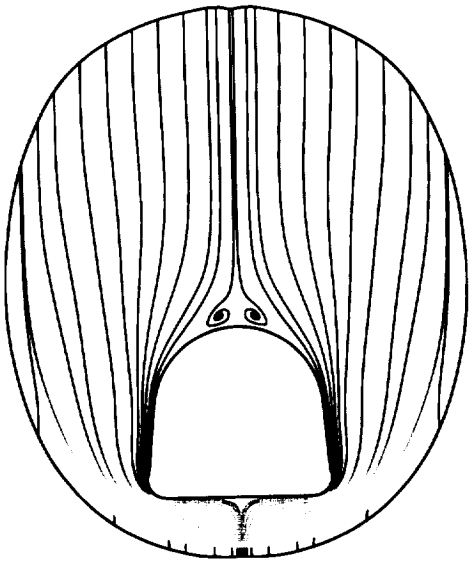

c) Before strake begins (x/L=0.29).

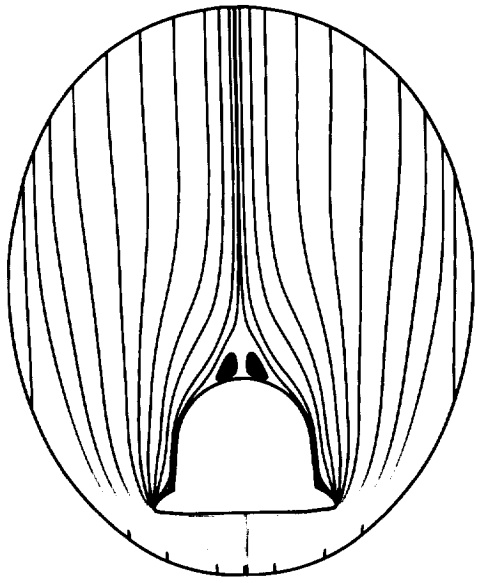

d) On strake (x/L=0.39).

Figure 5. Cross-flow streamlines colored by pressure (Case 1b).

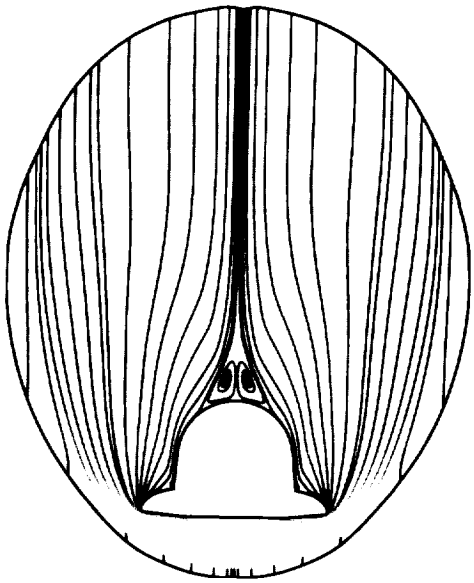

e) Before strake-wing juncture (x/L=0.46).

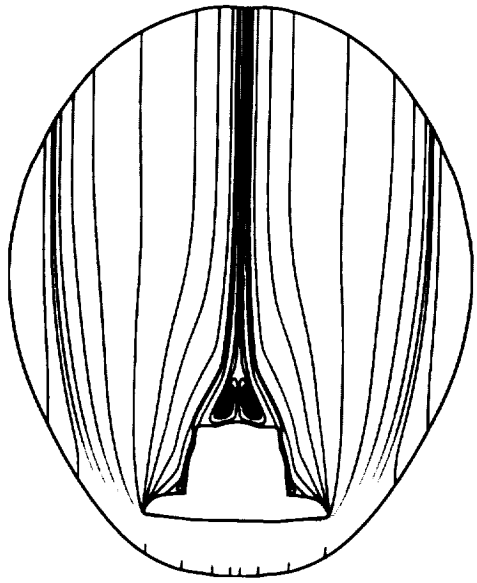

f) Fuselage cross-section transition (x/L=0.54).

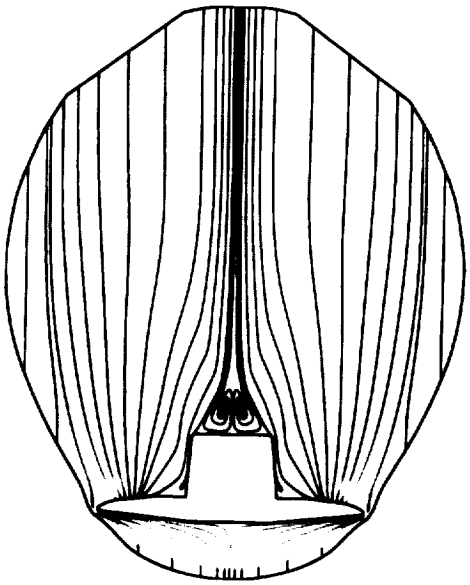

g) After fuselage cross-section transition (x/L=0.61).

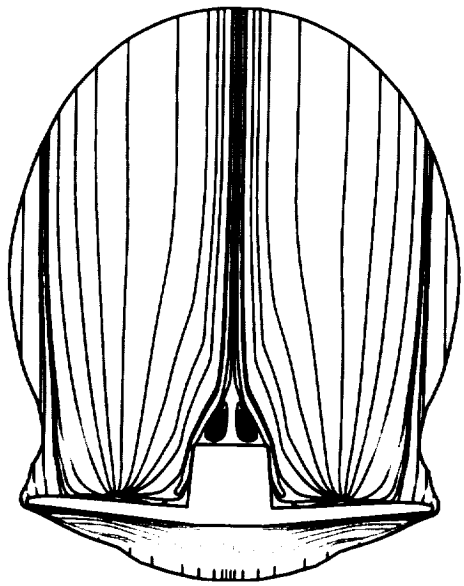

h) Just onto wing tip (x/L=0.71).

Figure 5. Continued.

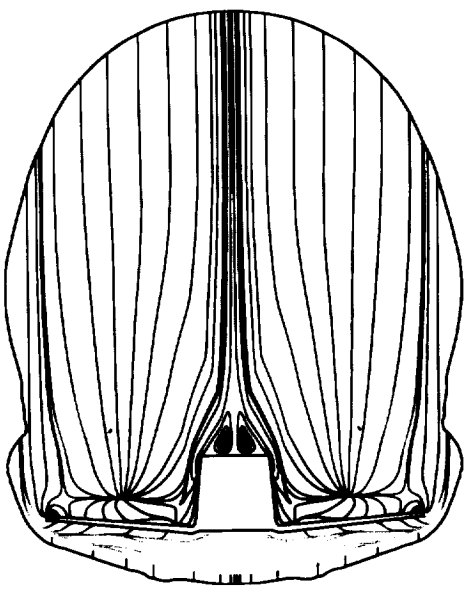

i) Before wing trailing edge (x/L=0.79).

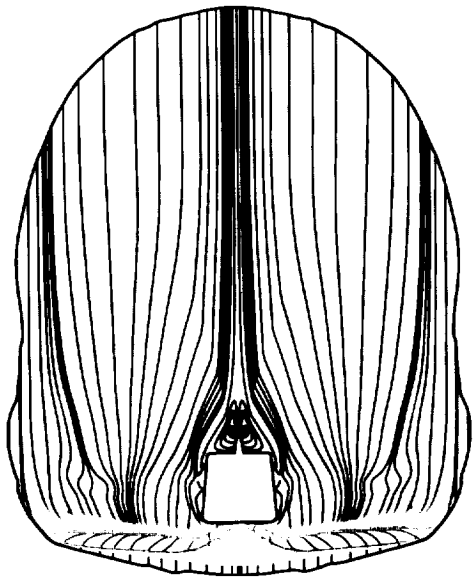

j) Behind wing trailing edge (x/L=0.86).

Figure 5. Concluded.

Next, the flow field in the vicinity of the body flap is examined with Figs. 7 and 8. Looking from the underside of vehicle, Fig. 7 shows the view in the vicinity of the body flap notch region. The vehicle extends off to the right and the rest of the body flap continues to the left. The back surface of the vehicle is truncated due to the limited computational domain used to model this region. Near-surface streamlines are shown colored by pressure variation. A re-attachment line is clearly evident along the leading edge of the body flap notch. This is created by the flow expanding around the bottom, aft corner of the vehicle. In fact, as shown by the series of span-wise cross-sectional cuts of density contours in Fig. 8, the flow is strong enough to create an embedded shock along the leading edge of the body flap notch. For this figure, the viewpoint is from the top of the wing, looking aft towards the side of the body flap (the body and body flap surfaces have been removed). The first cross-section contains the aft end of the vehicle, with the following cross-sections in the notched area, and the last cross section just after the body flap regains its full span.

Note: since the grid topology in the notch region was such that it was not possible to run the notch block with the algebraic turbulence model as implemented, this block was run using the laminar Navier-Stokes equations. As a consequence, any surface wetted by flow emanating from the notch region has erroneous surface temperatures. However, from investigations comparing the purely laminar results and the mixed turbulent-laminar results, the basic flow structure in this area remains un-effected. This is fortunate since Fig. 7 shows

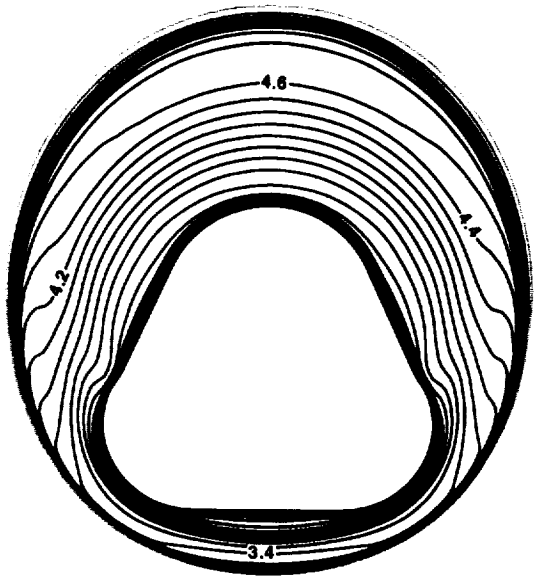

a) Downstream of spherical nose cap (x/L=0.04).

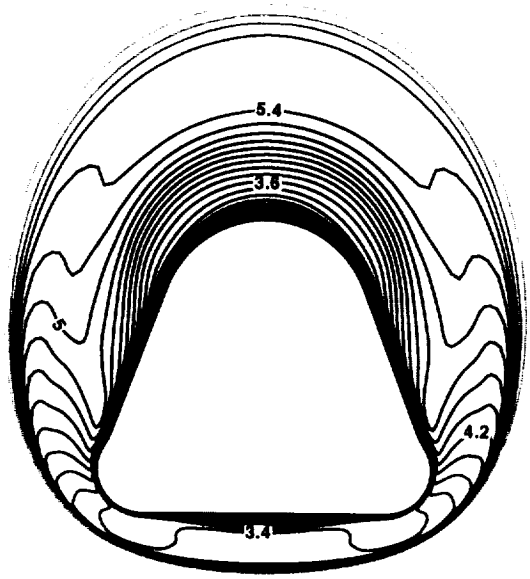

b) Canopy region (x/L=0.11).

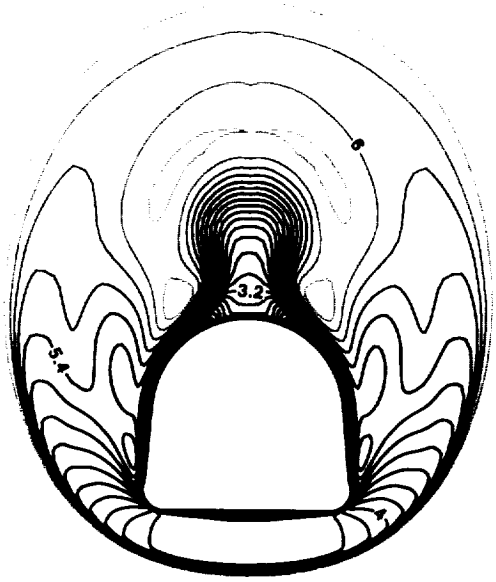

c) Before strake begins (x/L=0.29).

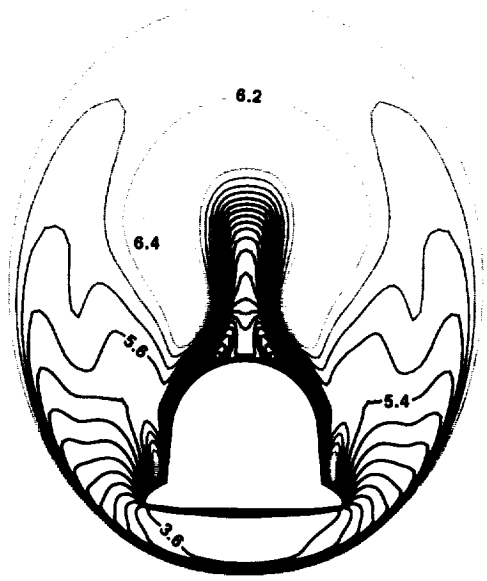

d) On strake (x/L=0.39).

Figure 6. Mach contours (ΔM=0.2, Case 1b).

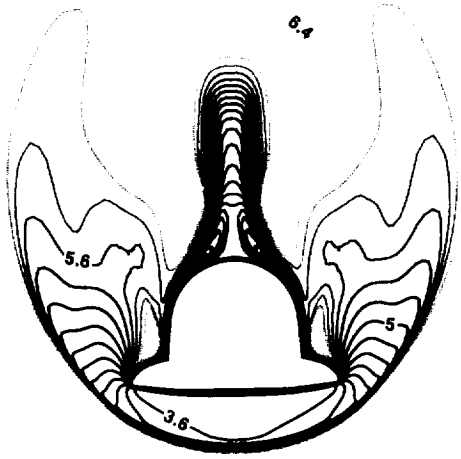

e) Before strake-wing juncture (x/L=0.46).

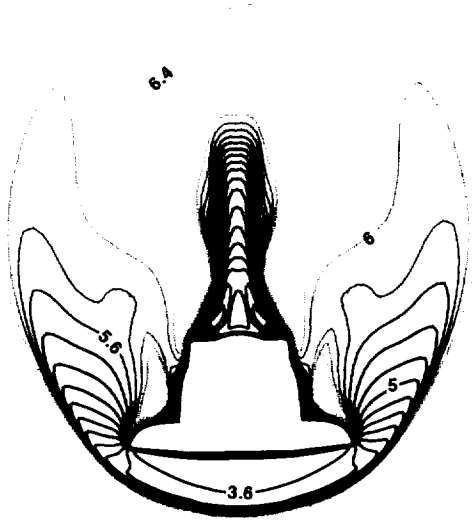

f) Fuselage cross-section transition (x/L=0.54).

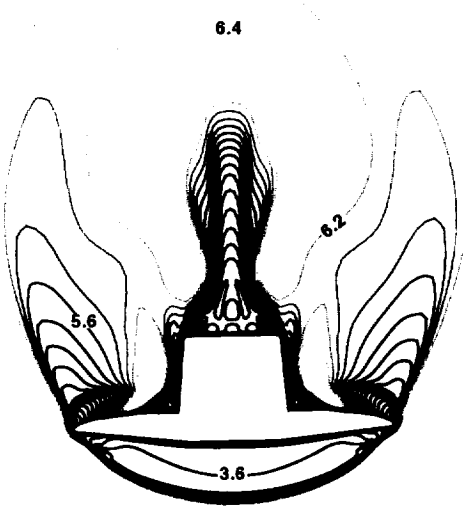

g) After fuselage cross-section transition (x/L=0.61).

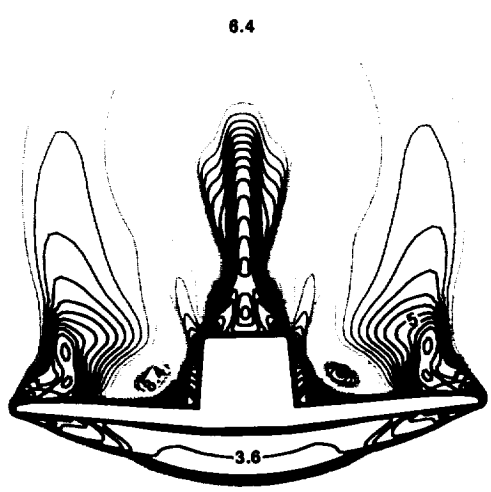

h) Just onto wing tip (x/L=0.71).

Figure 6. Continued.

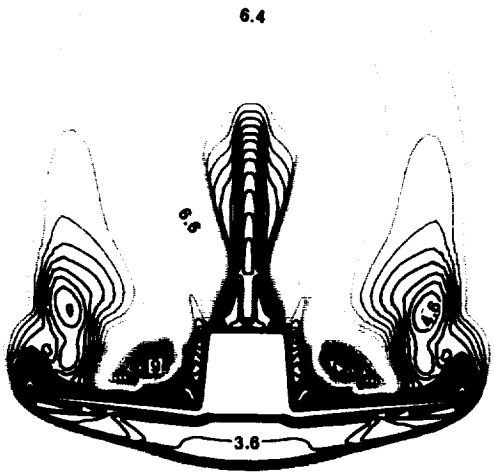

i) Before wing trailing edge (x/L=0.79).

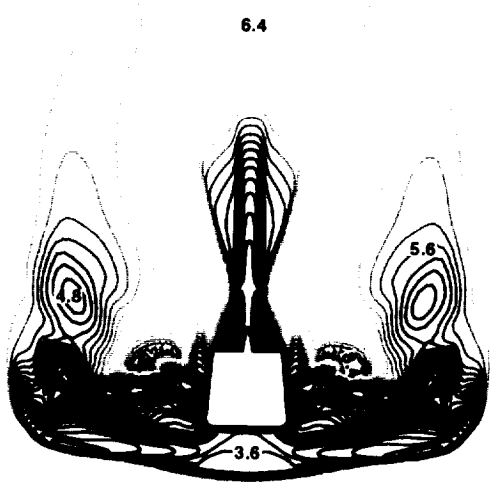

j) Behind wing trailing edge (x/L=0.86).

Figure 6. Concluded.

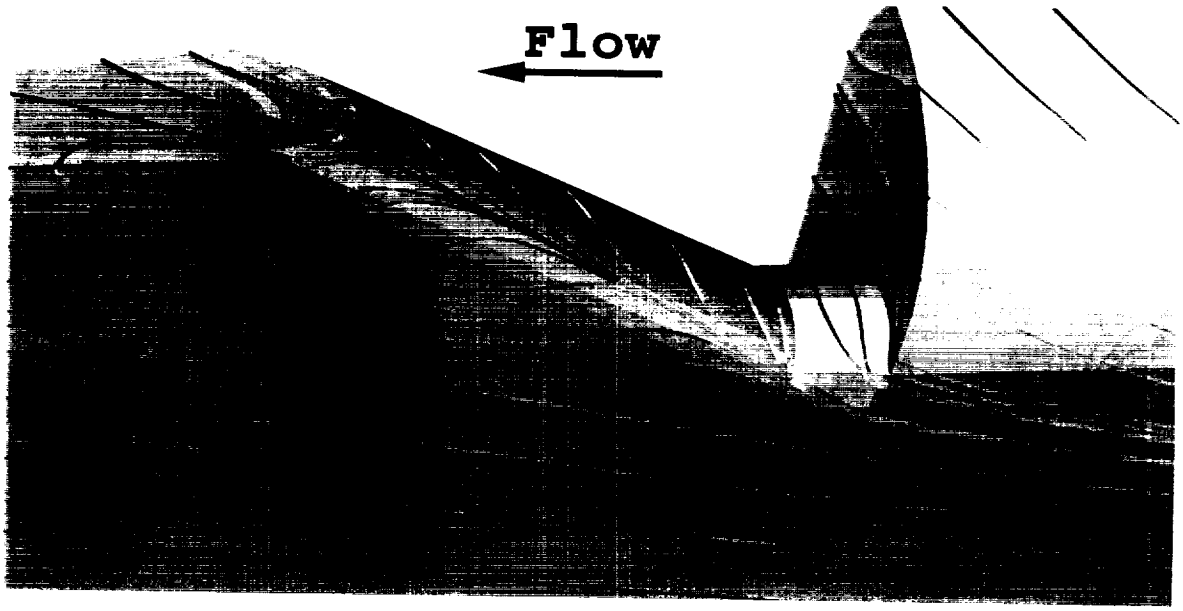

Figure 7. Streamlines colored by pressure in the vicinity of the body flap notch (Case 1a).

Figure 8. Span-wise cross-sectional cuts showing density contours along the aft of the vehicle and the body flap (Case 1a).

that there is a dividing streamline between the flow which remains on the wind side and the flow which travels onto the side wall and then returns to the wind side. This serves to limit the contamination caused by the embedded laminar block.

Surface Shear Patterns—Comparison with Experiment

Computer-simulated near-surface streamlines at flight conditions are shown in Fig. 9 for Case 2a, assuming a turbulent boundary layer. Figure 10 shows the corresponding oil flow from a Mach 10 wind-tunnel run where the attached flow over model is assumed to be laminar.[13] While Mach 6 wind tunnel results are also available, the Mach 10 data was chosen for comparison since the normal-shock density ratio is more comparable to the flight condition.

Comparing wind-side flow features, both datasets show similar indications of wind-side vortex patterns (refer to Fig. 5(a)) scrubbing the boundary layer toward the centerline on the forward quarter of the vehicle. Forced by a span-wise pressure gradient generated by the nose geometry which transitions from a spherical cross section to a rounded, triangular shape, the wind-side flow is initially converging toward the centerline. After a quarter of the vehicle, the centerline boundary layer has thickened and these wind-side vortices dissipate, establishing the streamline patterns containing an outboard component that dominate the surface flow over the latter three-fourths of the vehicle. The surface discontinuity at the wing-fuselage junction gives rise to a slight change in the streamline patterns, more visible

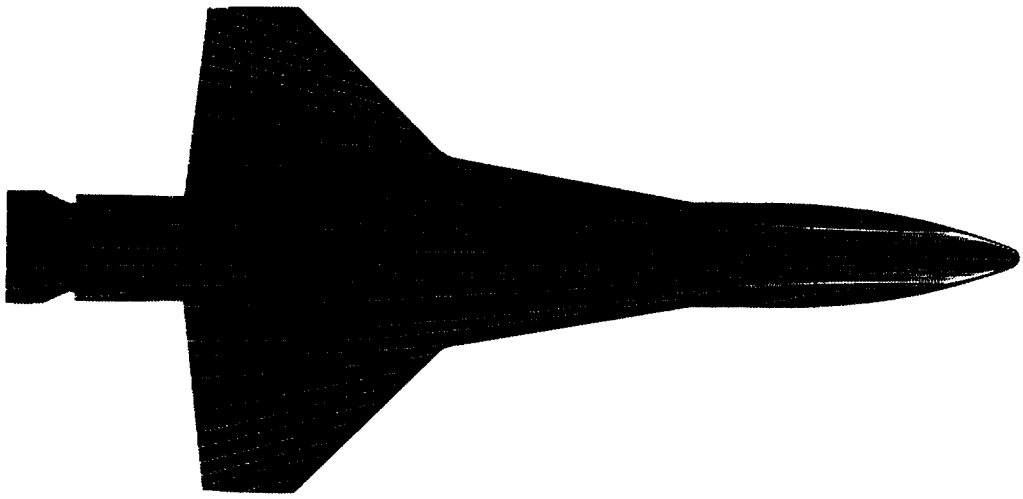

a) Wind side.

b) Starboard side.

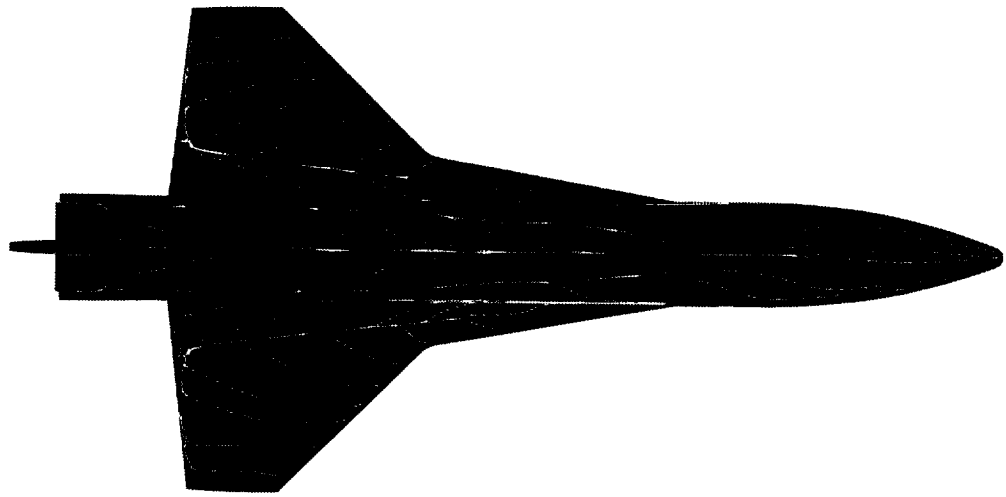

c) Lee side.

Figure 9. Computed near-surface streamlines (Case 2a).

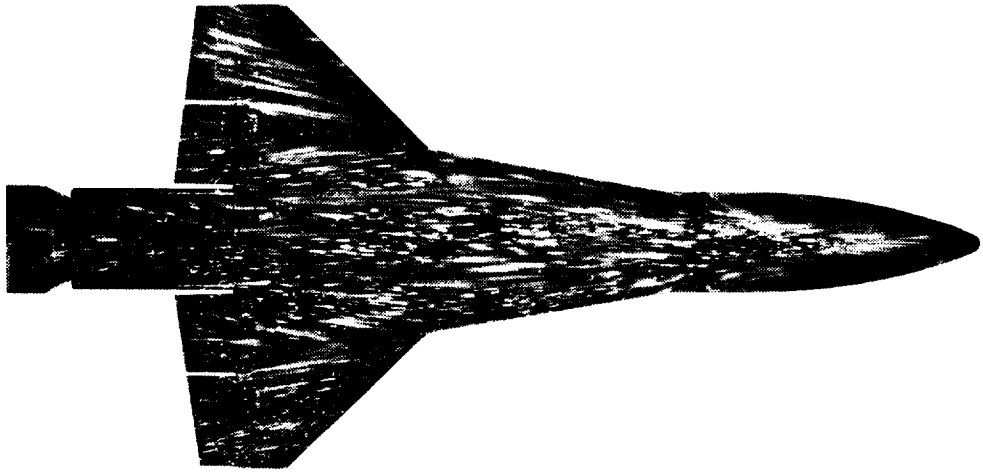

a) Wind side.

b) Starboard side.

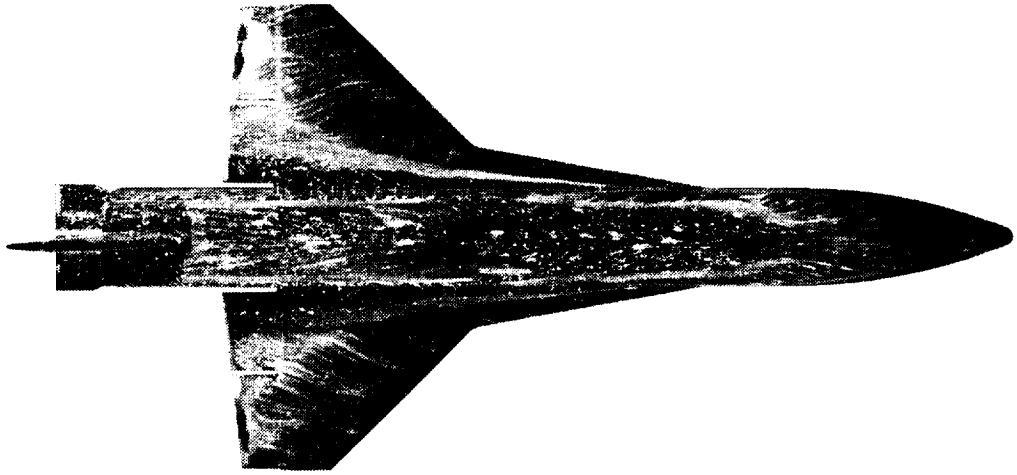

c) Lee side.

Figure 10. Oil flow for Mach 10 conditions from Ref. 13 ($\alpha = 15$ deg., $Re_\infty = 1.0 \times 10^6$).

in the experimental results. Both datasets show a divergence of streamlines emanating from the wing-strake joint which is next to the bow-shock impingement region. The experimental streamlines at the wing trailing edge show some localized behavior due to the elevon gaps, not present in the computational results, which did not model the elevon gaps.

Side-view comparisons show very good agreement, particularly in the forebody patterns. Both datasets show a strong cross-flow shock location and the separation line on the fuselage caused by the vortex emanating from the strake. A strong interaction region is seen, particularly in the computational solution, on the fuselage aft of the wing trailing edge. There is a bleed-through effect in this region on the experimental model due to the elevon gap, which is not modeled in the numerical simulation.

Lee-side surface features are in good agreement between the datasets, showing the strong cross-flow shock separation on the fuselage and the strake vortex across the wing, close to the fuselage. Inboard flow is seen over much of the wing while the fuselage shows outboard flow, generated by a longitudinal recirculation zone. Turning and separation, with a probable horse-shoe vortex, occurs in front of the vertical tail.

Further comparisons with experimental data are available in Ref. 13.

Surface Temperatures

This section presents the surface temperatures for all turbulent boundary-layer cases computed: Cases 1a, 1b, 2a, and 2b. Discussion includes the effects of angle-of-attack variation and control surface deflections.

Case 1a: Figure 11 shows surface temperature contours[j] for Case 1a. The wind-side view shown in Fig. 11(a) shows the expected high temperatures for the nose stagnation region. The forebody chines also show significant temperature elevation due to the vehicle's forebody geometry approaching the bow shock generated by the spherical nose cap. Also present on Fig. 11(a) are streaks of elevated temperatures crossing the wings chord-wise. This corresponds to the remnants of the forebody bow shock (*cf.* Fig. 4(a)). Also, although not readily discernible with this choice of temperature contour levels, there is a second streak emanating from the bow shock-wing shock interaction point just outside of the wing/strake juncture, raked aft from the leading edge of the wing. This second streak is readily apparent in the experimental results of Ref. 13. The vast acreage of the wind-side fuselage surface is in the range of 1300-1400 °F.

Note that the outside edges of the body flap have slightly cooler temperatures than the inboard portion. This area of cooler temperatures is associated with near-surface streamlines

[j]Note that there are three contour-level legends in the figure, one for each of the lee-side, starboard, and wind-side views; but these same three contour level distributions are held constant for all subsequent surface temperature figures to facilitate comparisons.

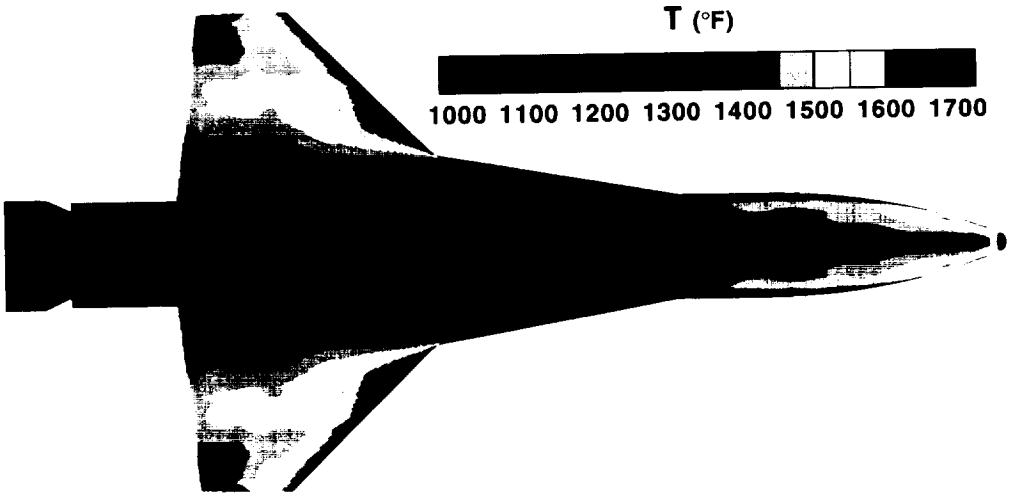

a) Wind side.

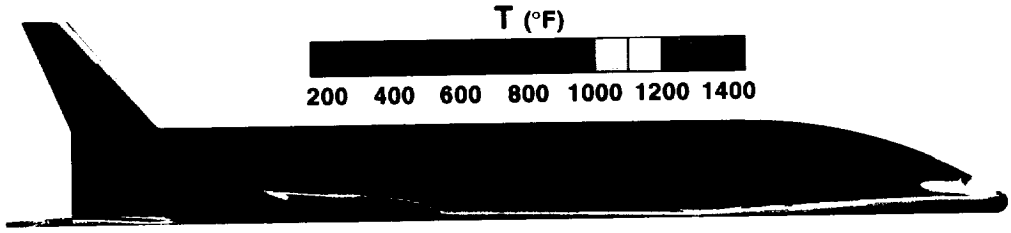

b) Starboard side.

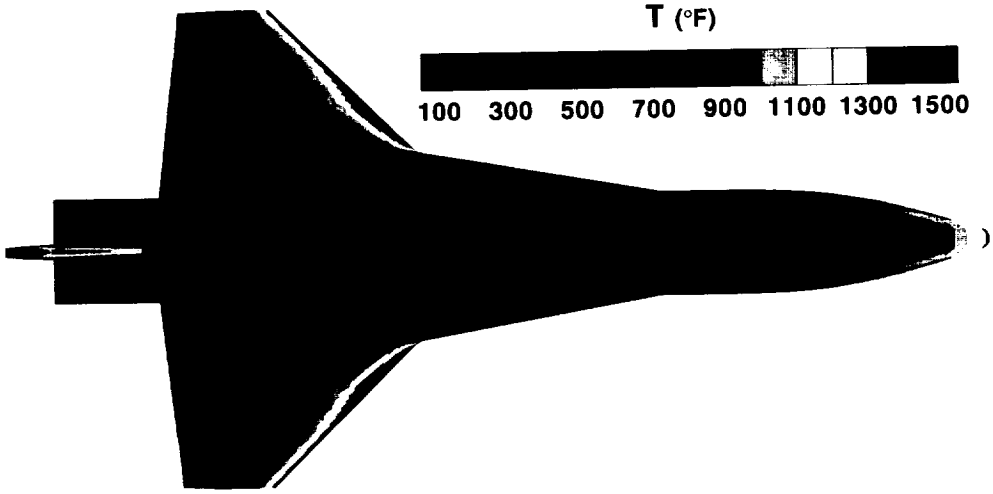

c) Lee side.

Figure 11. Surface temperatures (Case 1a).

that emanate from the leading edge of the notched body flap. This is trend is erroneous as discussed on page 13.

The starboard and lee-side views (Figs. 11(b) and 11(c)) show the effects of several flow features previously discussed. For instance, between the canopy and the round-to-squared fuselage transition, longitudinal low-temperature streaks are well defined, corresponding to the pair of vortices located just above the fuselage. As mentioned previously on page 10, when the fuselage cross-section transition is encountered, an embedded shock is generated which is indicated by the triangular-shaped region of higher temperatures in this area.

Case 1b: Surface temperatures for the deflected control surface case (1b), are shown in Fig. 12. As compared to the undeflected case, the temperatures on the forebody are not effected by the change due to fact that the shock layer has supersonic flow. As shown by Fig. 12(a) the deflected surfaces now experience 200-300 °F higher temperatures on their wind sides.

For this case, the non-physical effect of having to run the "notched" body flap region with the laminar equations is more readily apparent than for the undeflected case since the embedded body-flap-notch leading-edge shock (refer to Fig. 8) is stronger.

Although difficult to see in Figs. 11(b) and 12(b), the wing wake is slightly larger for the deflected case. Also, the footprint of the wing fish-tail shock is at a lower angle relative to the vehicle's longitudinal axis.

Case 2a: Surface temperatures for this lower-angle-of-attack case are shown in Fig. 13. As compared with Case 1, the wind-side temperatures are on the order of 250 °F lower while maintaining the same qualitative distribution, except for the wing-shock/bow-shock interaction occurring slightly closer to the fuselage. Figs. 13(c) and 13(b), however, show increased heating on the lee-side. Most notable are the nose region and the tail leading edge. The fuselage transition area is also slightly hotter. The wing-wake structure appears to have higher energy as its temperature footprints are on the order of a 100 °F higher than the higher-angle-of-attack case. The terminating fish-tail shock also appears stronger, reflected by its more oblique angle.

Case 2b: The effects of deflecting the elevon control surface 10 deg. are shown in Fig. 14. As for Cases 1a and 1b, the forward portion of the vehicle is not effected by this change due to supersonic flow, and the deflection simply results in higher wind-side temperatures for the flap (see Fig. 14(a)). However, for this lower angle-of-attack case, there is a small area of flow separation near the outboard end of the elevon, resulting in slightly lower temperatures in this area. This is faintly visible in Fig. 14(a) as a sliver of blue along the hinge line between 70 and 80% span. Its presence is more clearly indicated by the convex shape of the yellow-green contour level on the elevons in this region.

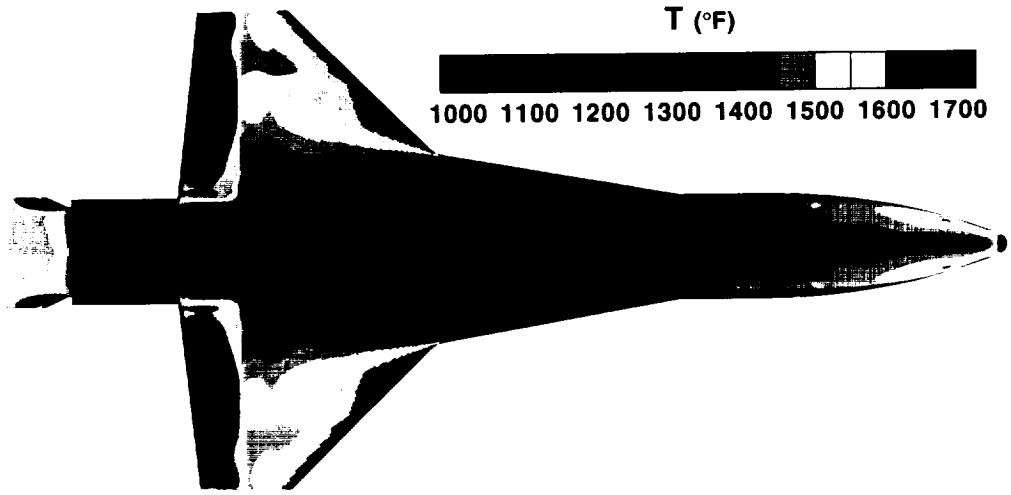

a) Wind side.

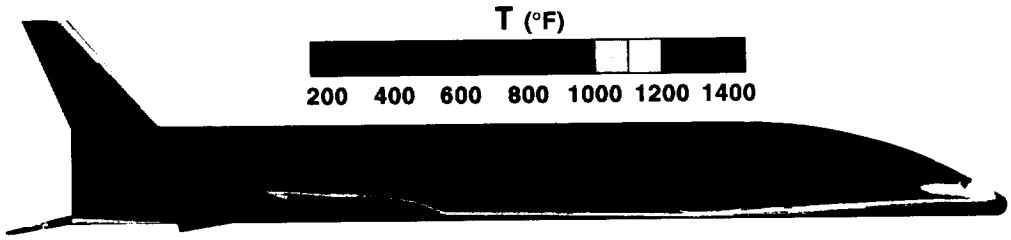

b) Starboard side.

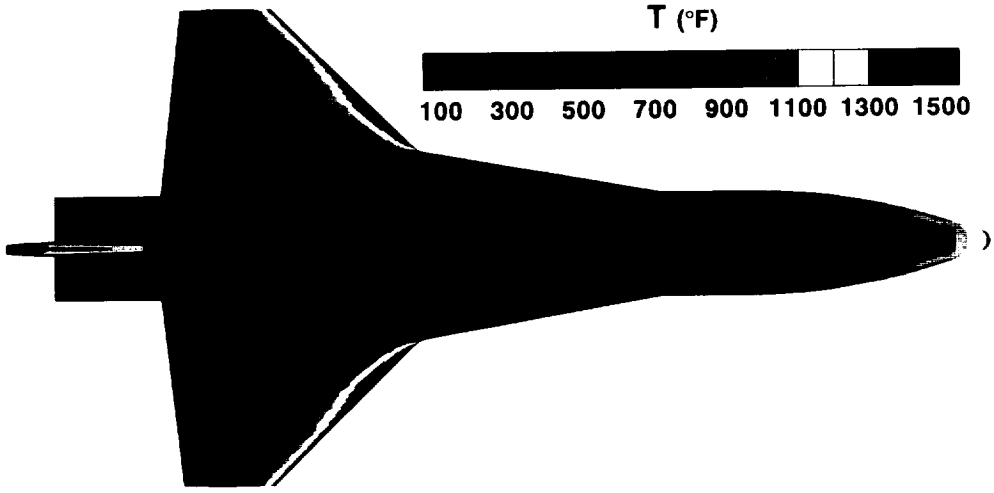

c) Lee side.

Figure 12. Surface temperatures (Case 1b).

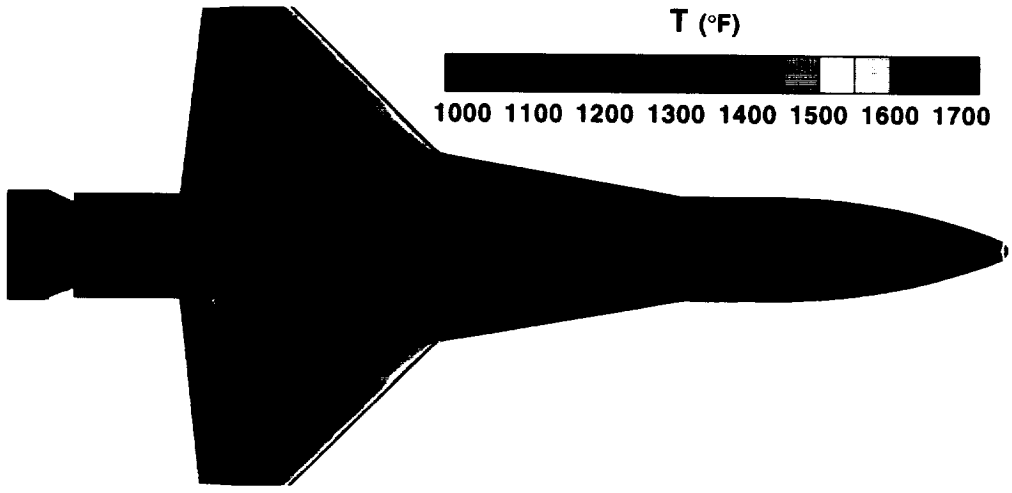

a) Wind side.

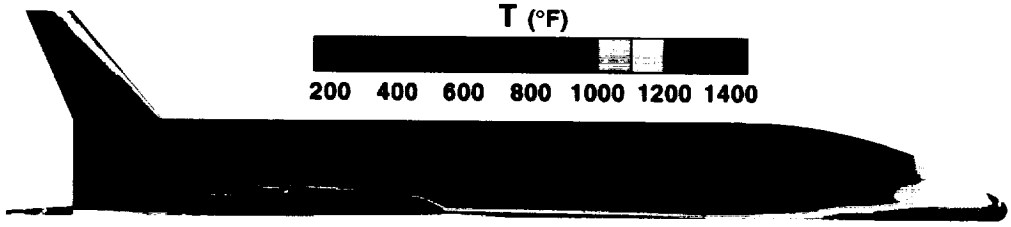

b) Starboard side.

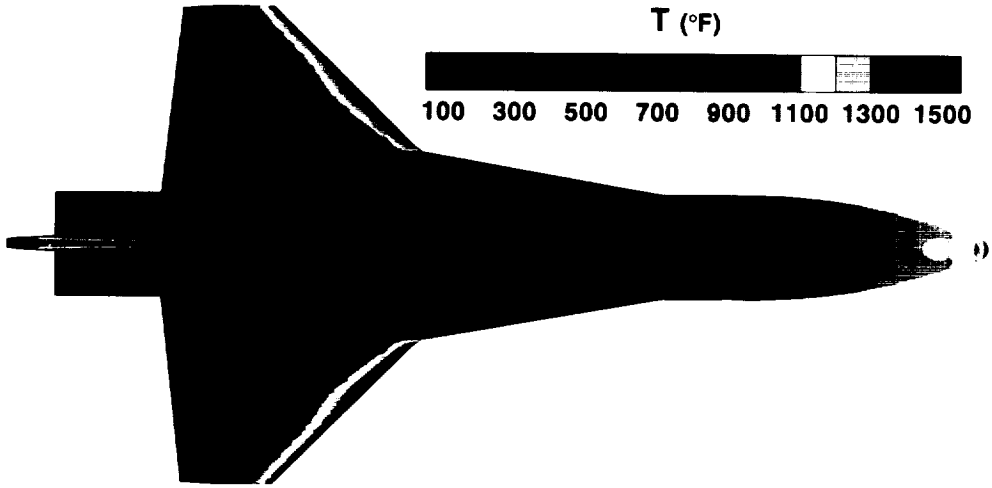

c) Lee side.

Figure 13. Surface temperatures (Case 2a).

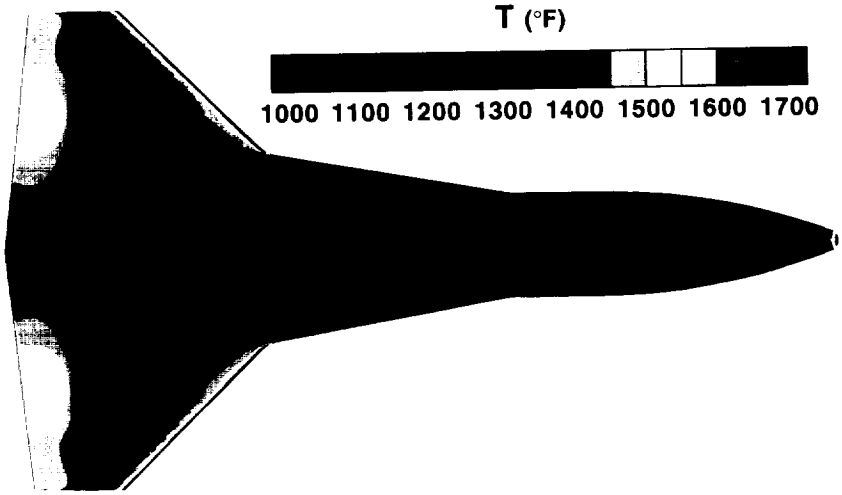

a) Wind side.

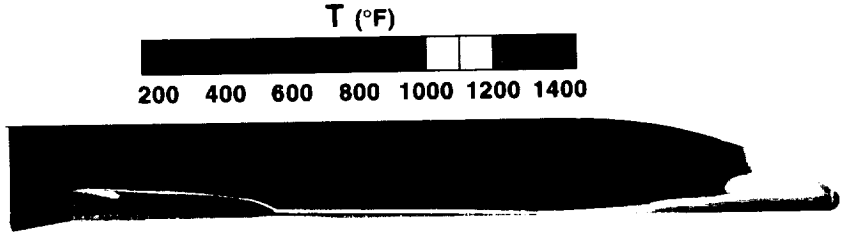

b) Starboard side.

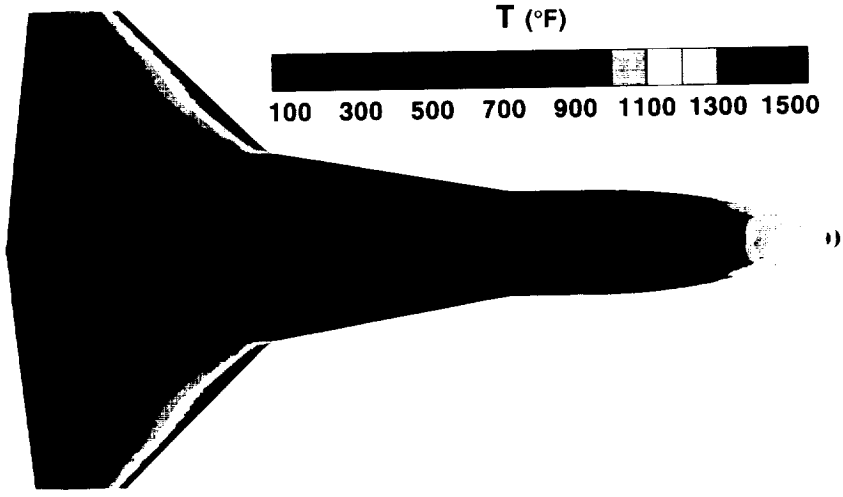

c) Lee side.

Figure 14. Surface temperatures (Case 2b).

Heating Rates

Figs. 11-14 have been presented in terms of temperatures since this is the most important quantity to consider when ensuring that no TPS temperature limits are violated. For the reader, estimates of the corresponding heating rates can be derived from the temperature distributions with Eq. 1.

An example of an actual heating rate distribution is shown in Fig. 15[k] for Case 2b. The heating-rate distributions for the remaining cases are presented in Figs. 16–18.

Boundary-Layer State

For Cases 1a and 1b, both laminar and turbulent boundary-layer solutions were obtained. This section provides a brief synopsis of the effects of the boundary-layer state, focusing on the deflected control surfaces case, Case 1b.

Figures 15 and 19 show surface heating rates for turbulent and laminar boundary layers, respectively. By comparing Figs. 15 and 19, it is immediately evident that the turbulent boundary-layer assumption provides a more conservative estimate of the heating rates than the laminar boundary layer. Overall, the laminar heating rates tend to be half of those for the turbulent boundary layer. However, the qualitative agreement is very close, signifying that most of the heating patterns are determined by "inviscid" flow features such as shocks and vortex cores.

Laminar heating results for Case 1a are presented in Fig. 20 while Figs. 21 and 22 show laminar temperature distributions for Cases 1a and 1b.

Figures 23–26 show turbulent pressure distributions for Cases 1a, 1b, 2a, and 2b, respectively while Figs. 27 and 28 show the laminar results for Cases 1a and 1b. Upon comparing Figs. 24(a) and 28(a) for Case 1b, only small changes in the pressure distributions on the wind side are evident. These are primarily due to the fact that the laminar boundary layer sustains a small separated region in front of the deflected control surfaces whereas the turbulent boundary layer does not. This moves the associated embedded shocks forward. On the lee side, Figs. 24(b), 24(c), 28(b), and 28(c) show the major differences to be in the footprint of the wing-strake vortex structure and the lack of the wing fish-tail shock signature on the side of the fuselage for the laminar case.

[k]The dashed pattern of very low heating rates apparent on the lee side of the fuselage (see Fig. 15(c)) is due to an instability of the Baldwin-Lomax turbulence model when coupled with the iterative, radiative-equilibrium wall boundary condition in a multiple-block context. An improved algorithm for determining the location of the maximum vorticity within the boundary layer eliminated this problem in subsequent runs. This particular case was not re-computed due to limited resources and the fact that most regions of interest are outside the domain of dependence.

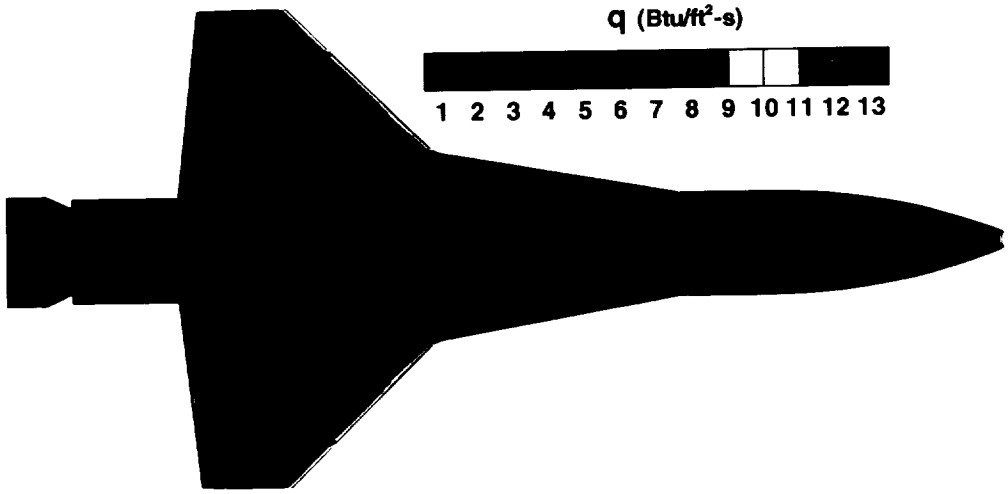

a) Wind side.

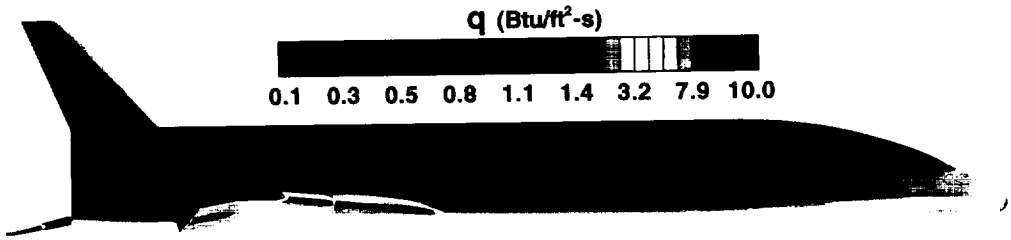

b) Starboard side.

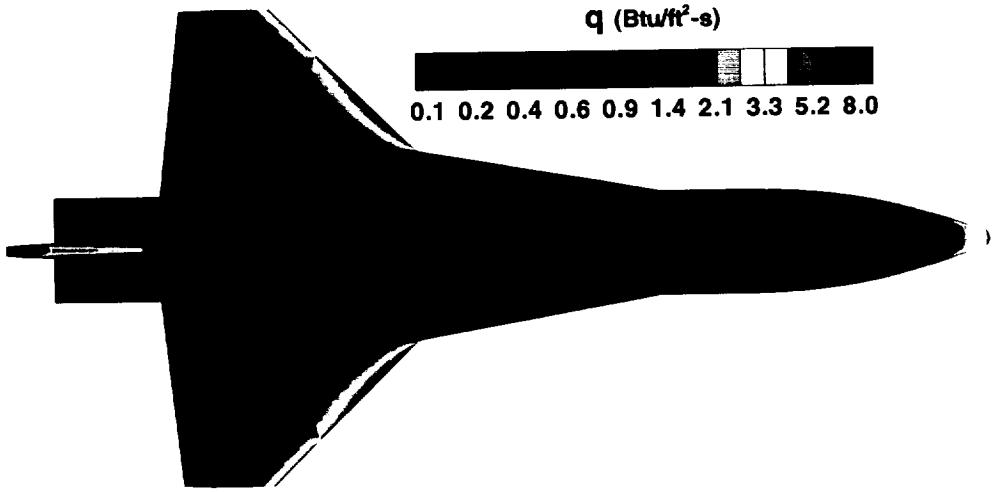

c) Lee side.

Figure 15. Heating rates (Case 1b).

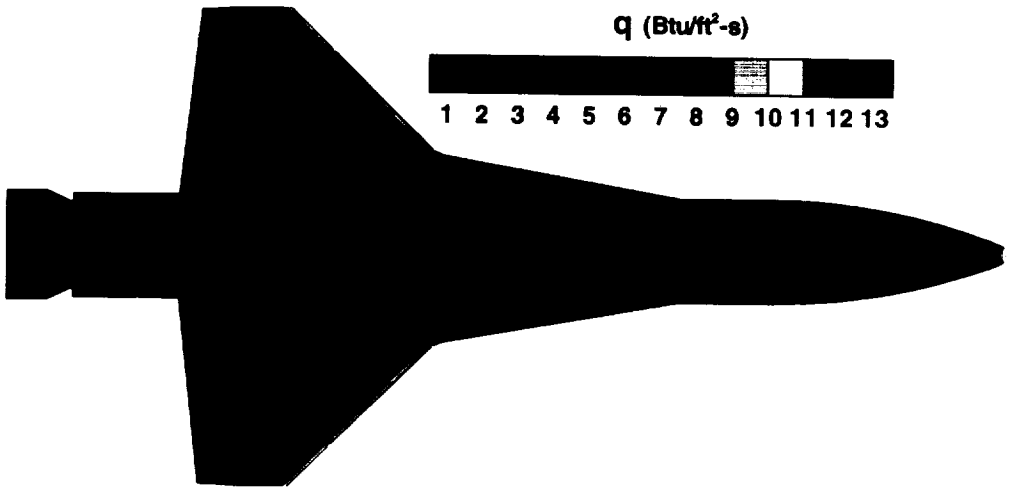

a) Wind side.

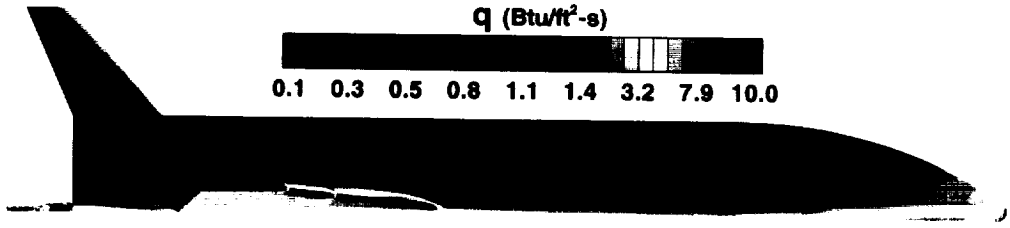

b) Starboard side.

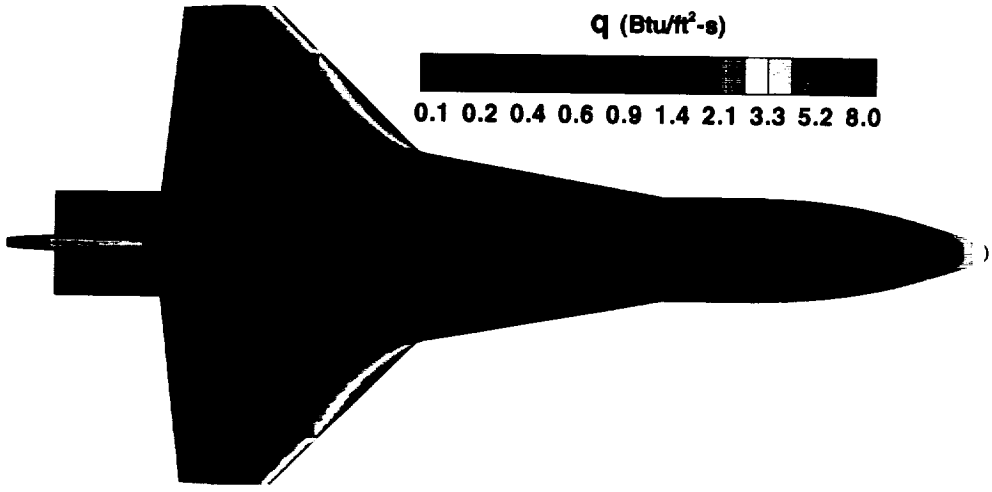

c) Lee side.

Figure 16. Heating rates (Case 1a).

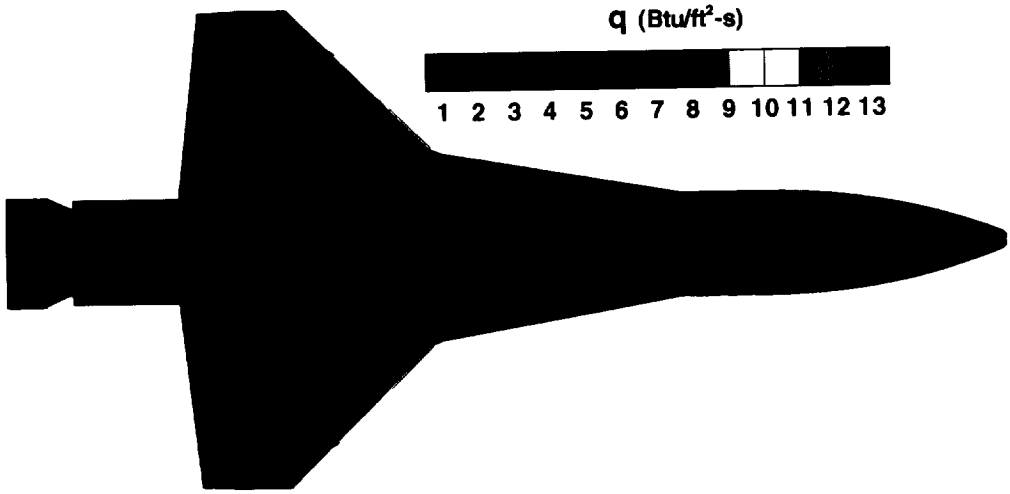

a) Wind side.

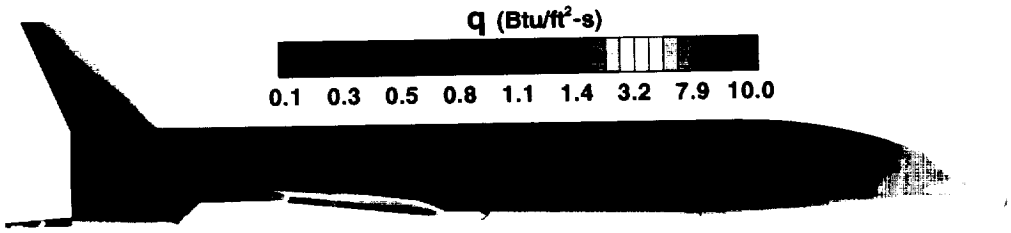

b) Starboard side.

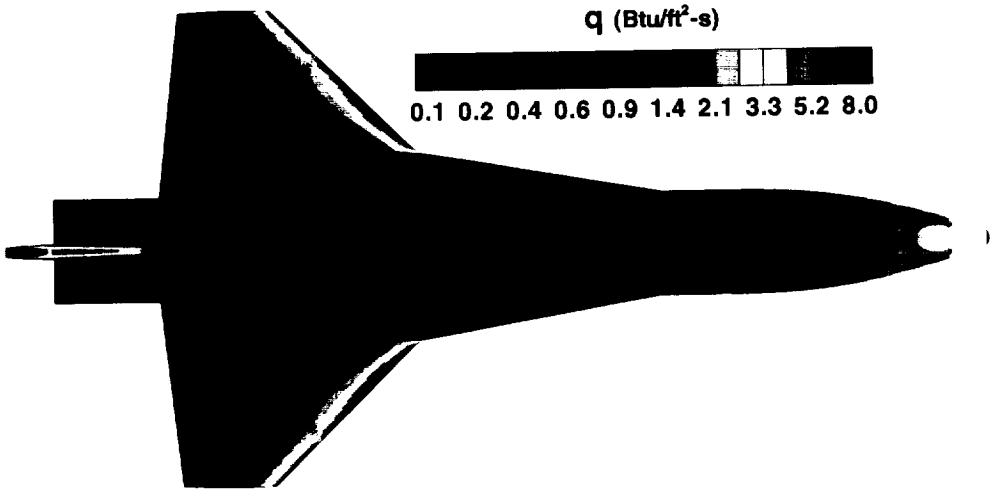

c) Lee side.

Figure 17. Heating rates (Case 2a).

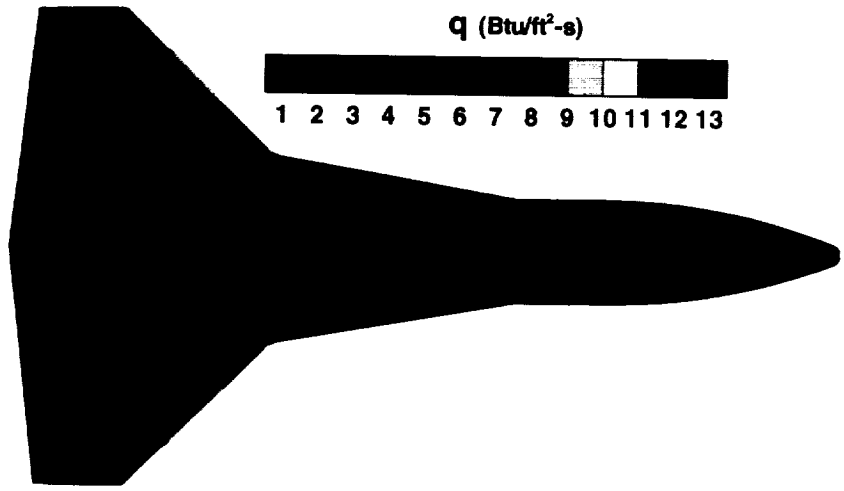

a) Wind side.

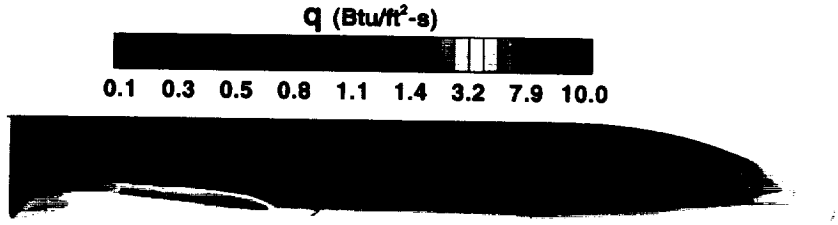

b) Starboard side.

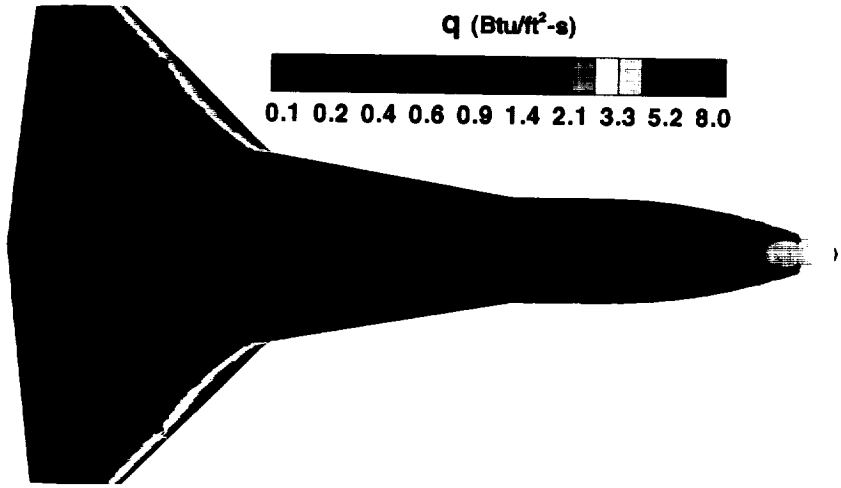

c) Lee side.

Figure 18. Heating rates (Case 2b).

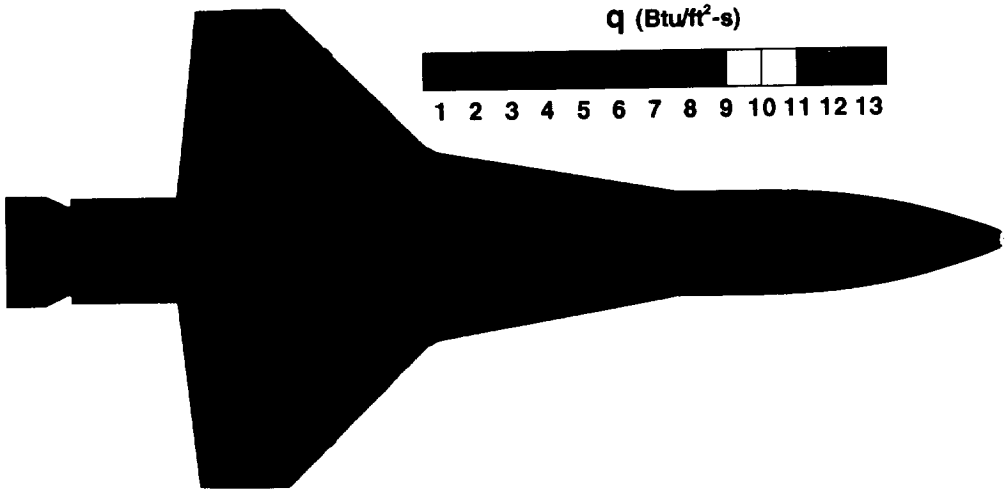

a) Wind side.

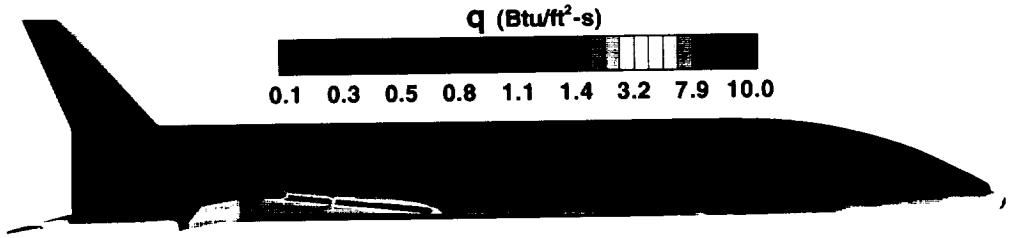

b) Starboard side.

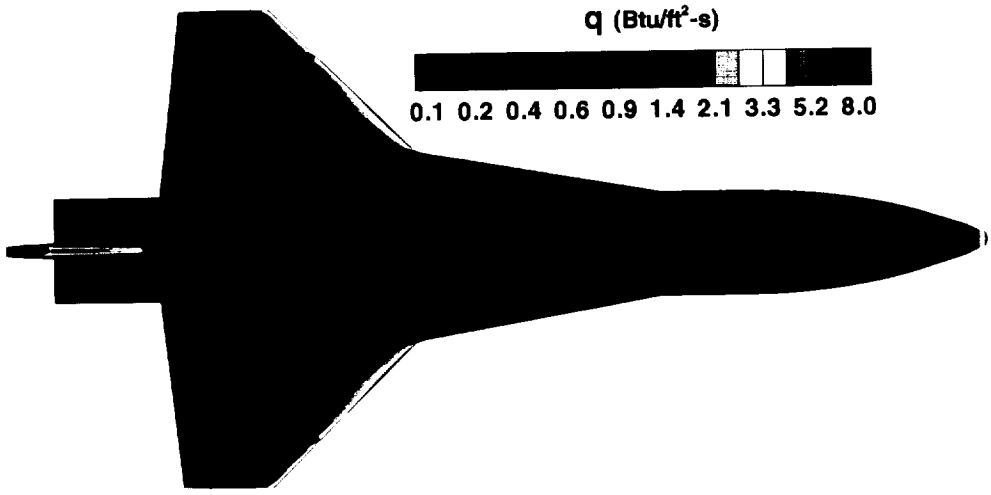

c) Lee side.

Figure 19. Heating rates (Case 1b), *laminar*.

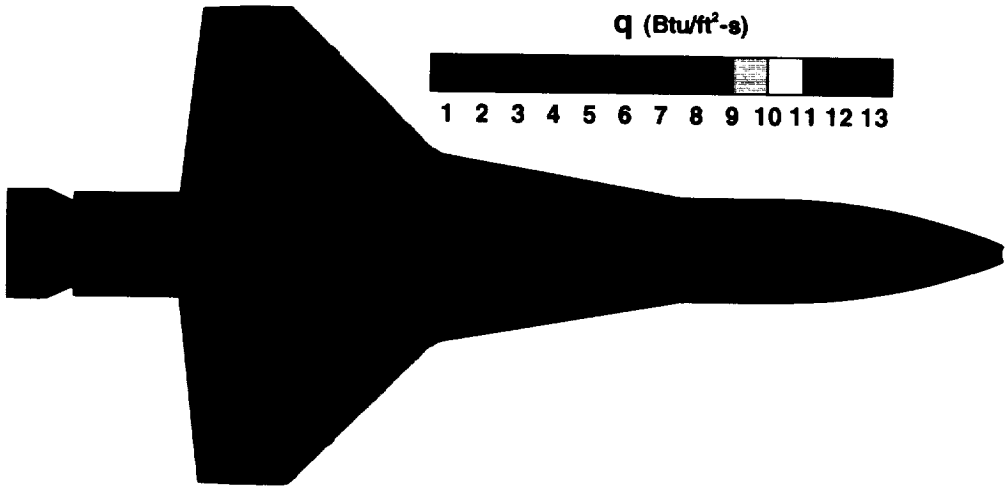

a) Wind side.

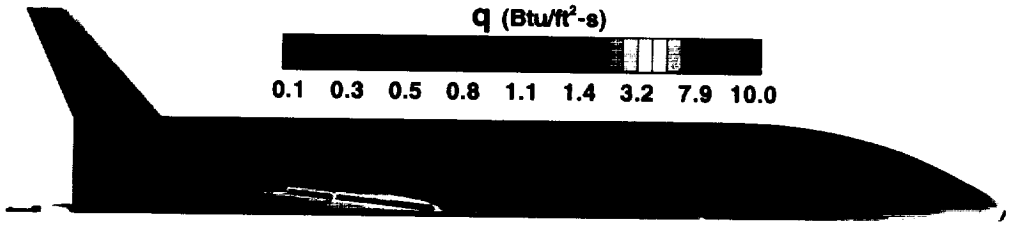

b) Starboard side.

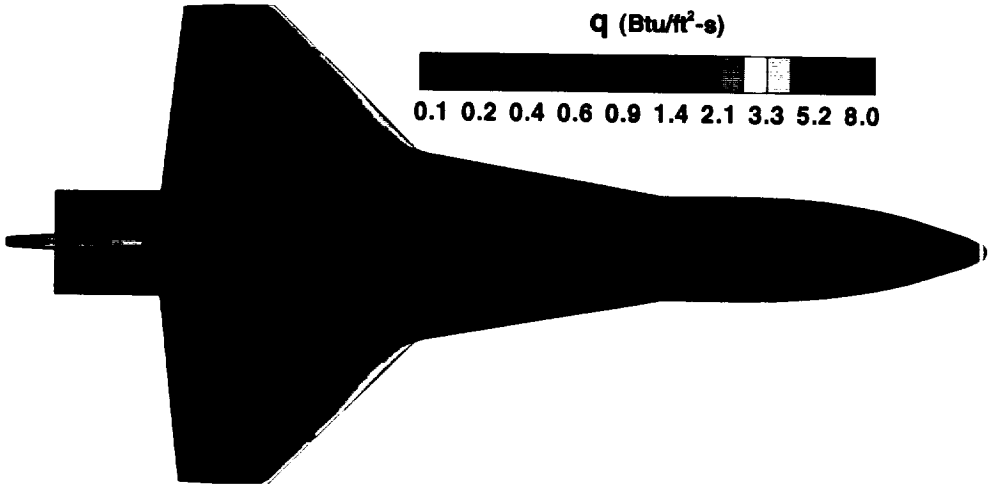

c) Lee side.

Figure 20. Heating rates (Case 1a), *laminar*.

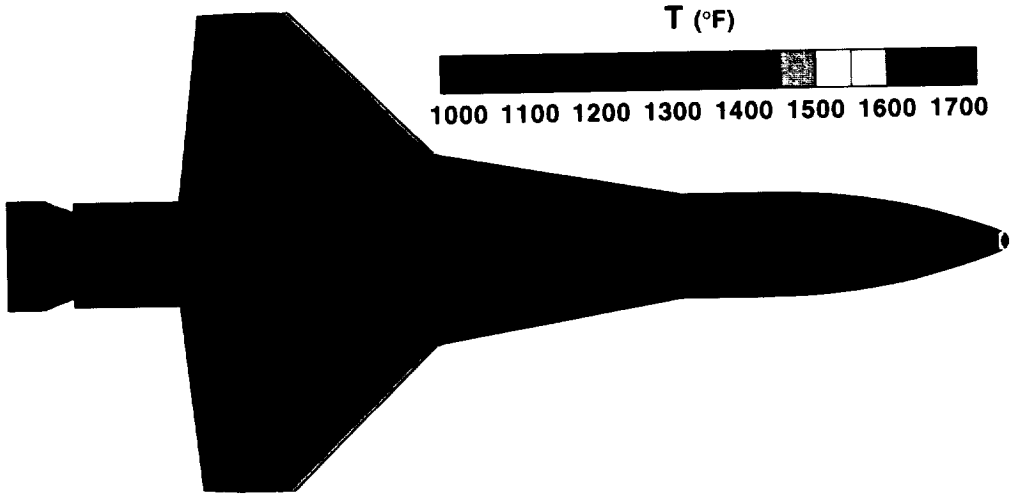

a) Wind side.

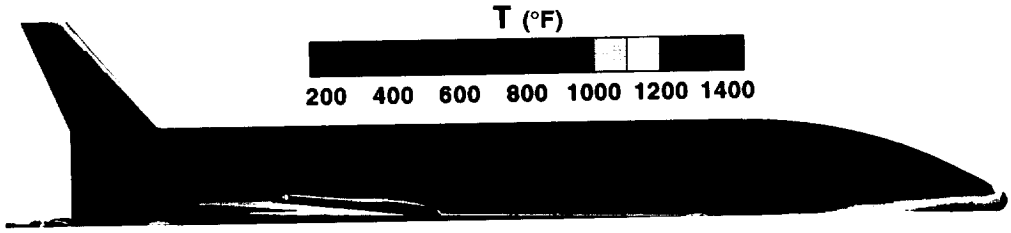

b) Starboard side.

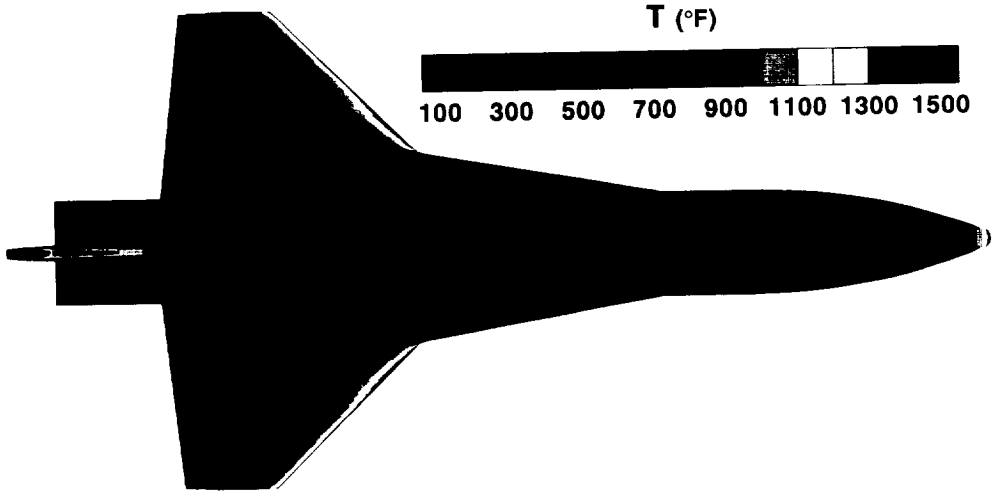

c) Lee side.

Figure 21. Temperature Distributions (Case 1a), *laminar*.

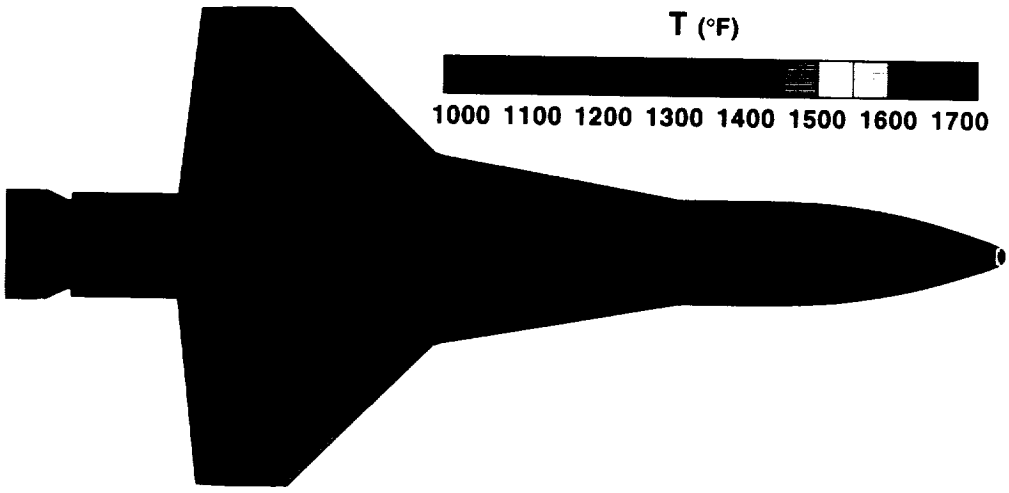

a) Wind side.

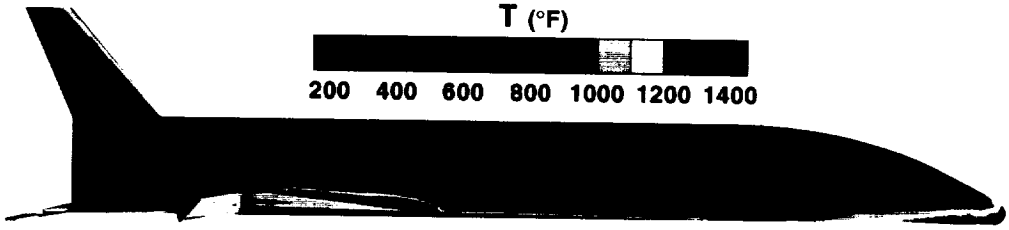

b) Starboard side.

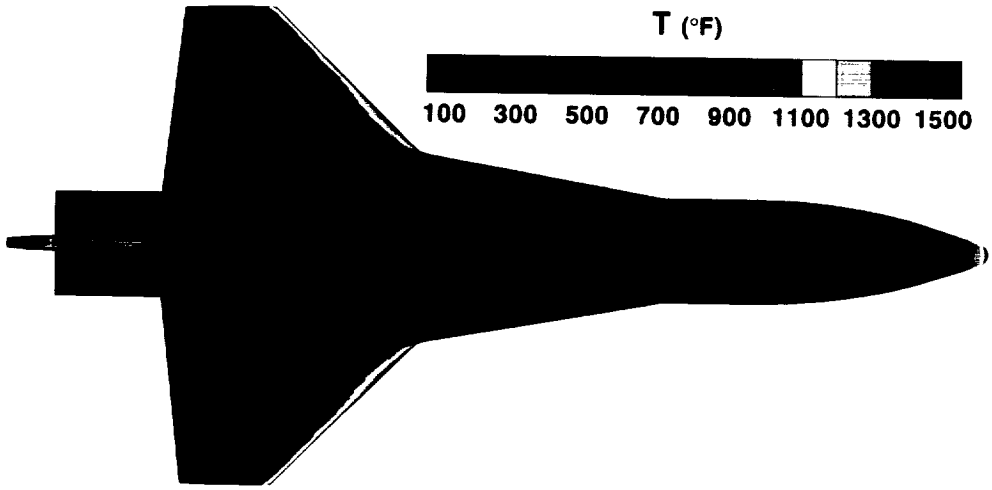

c) Lee side.

Figure 22. Temperature Distributions (Case 1b), *laminar*.

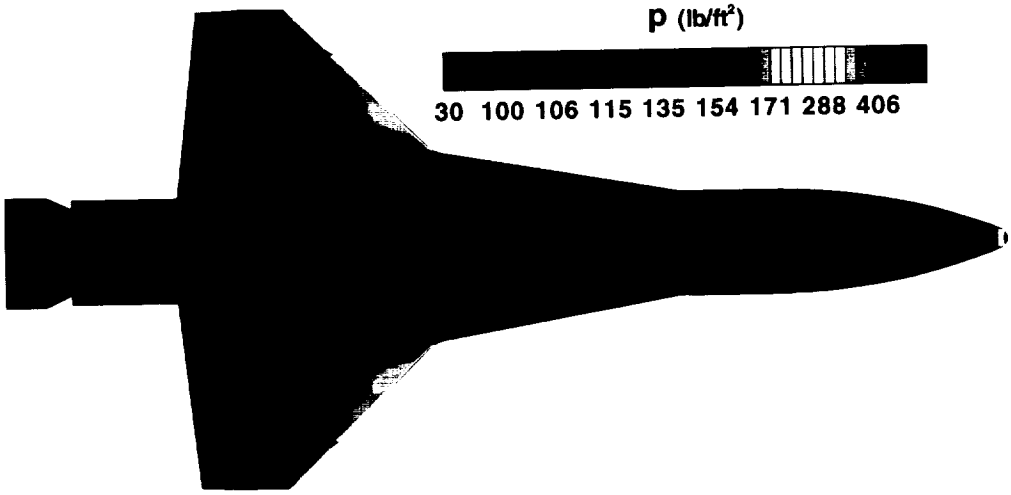

a) Wind side.

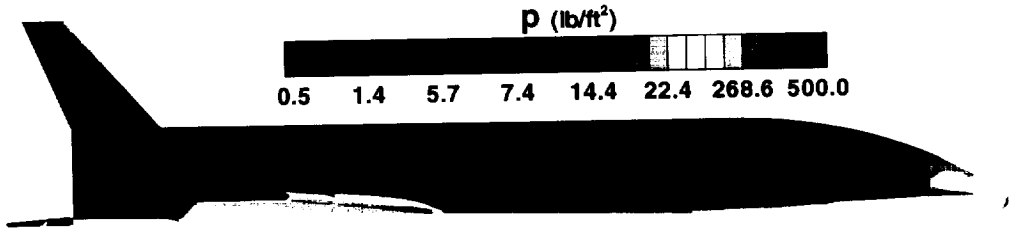

b) Starboard side.

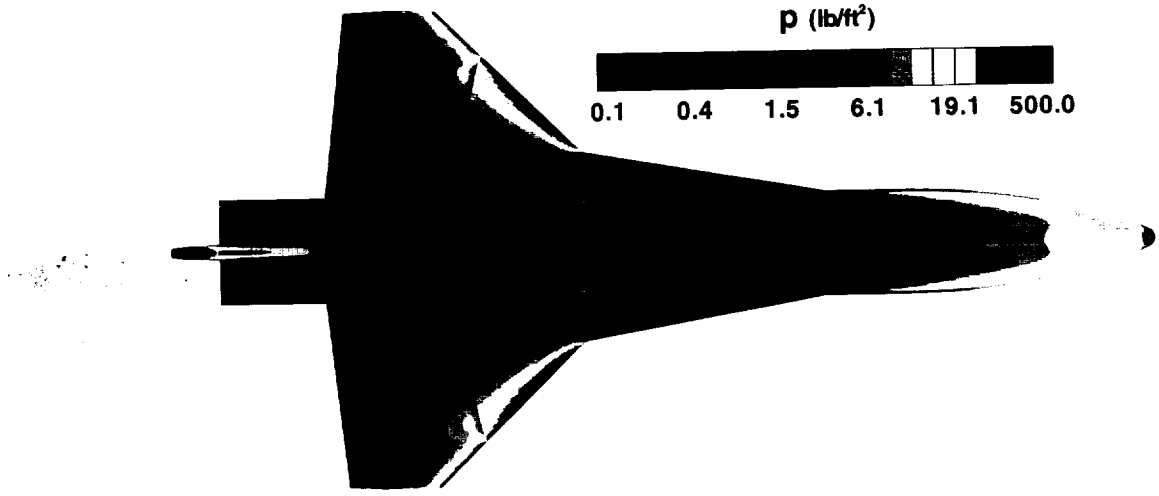

c) Lee side.

Figure 23. Pressure Distributions (Case 1a).

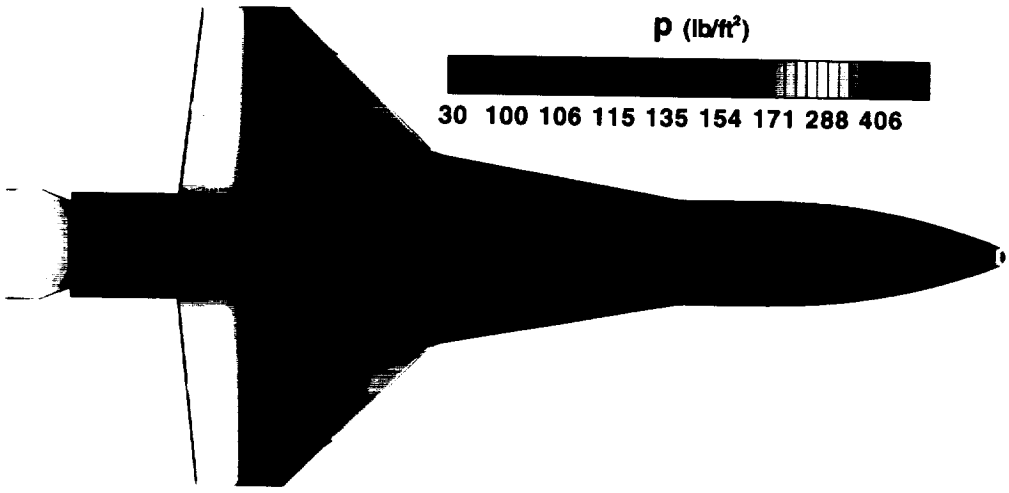

a) Wind side.

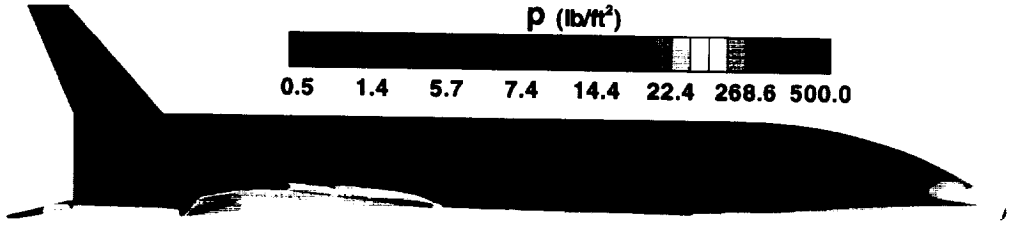

b) Starboard side.

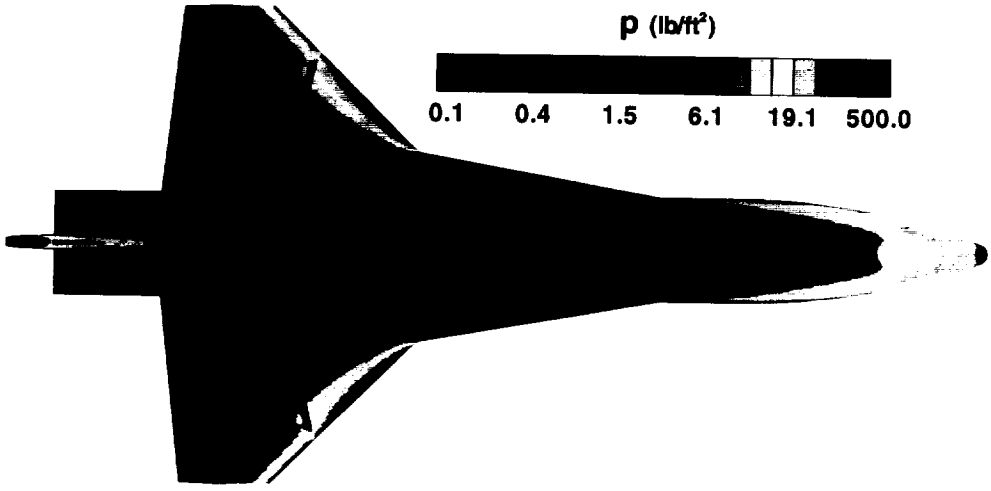

c) Lee side.

Figure 24. Pressure Distributions (Case 1b).

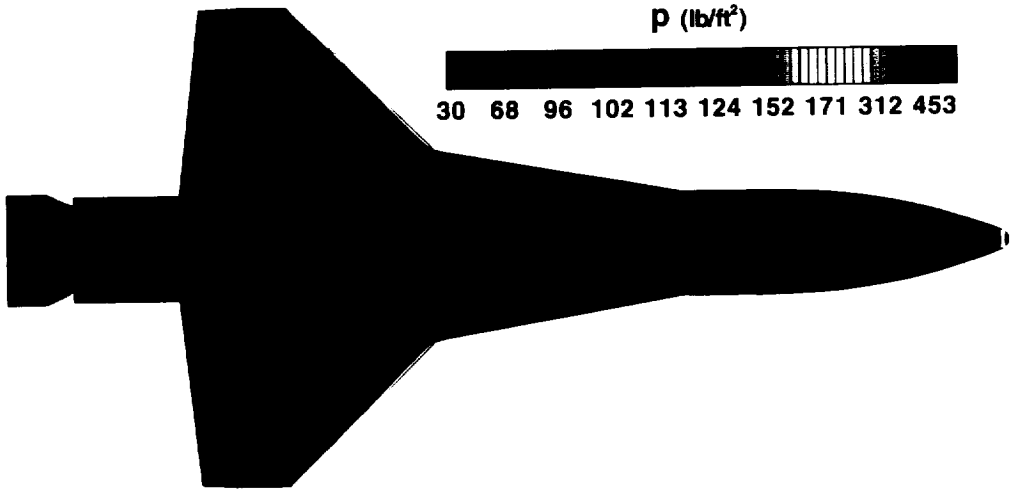

a) Wind side.

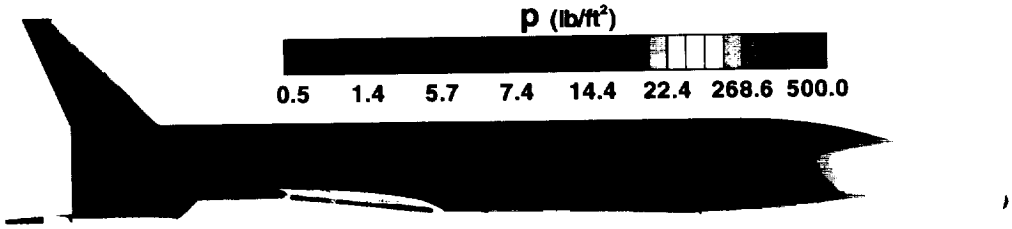

b) Starboard side.

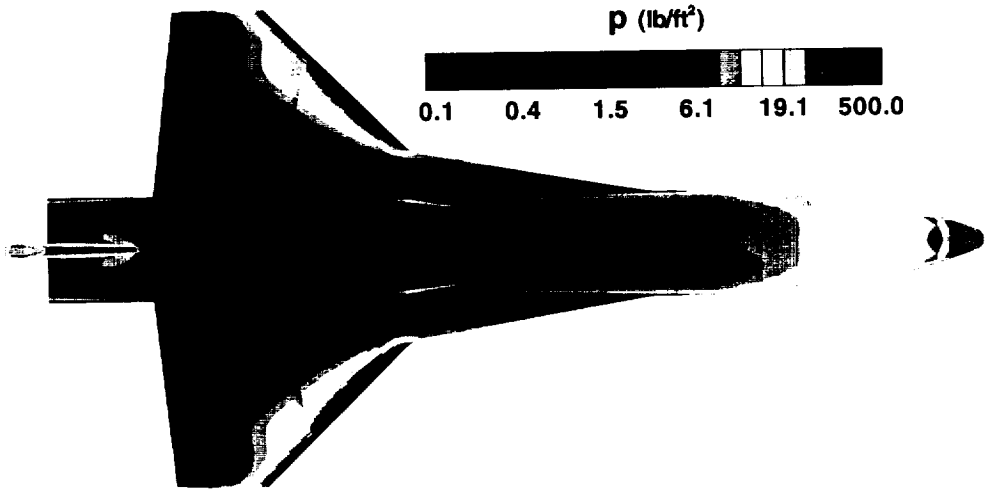

c) Lee side.

Figure 25. Pressure Distributions (Case 2a).

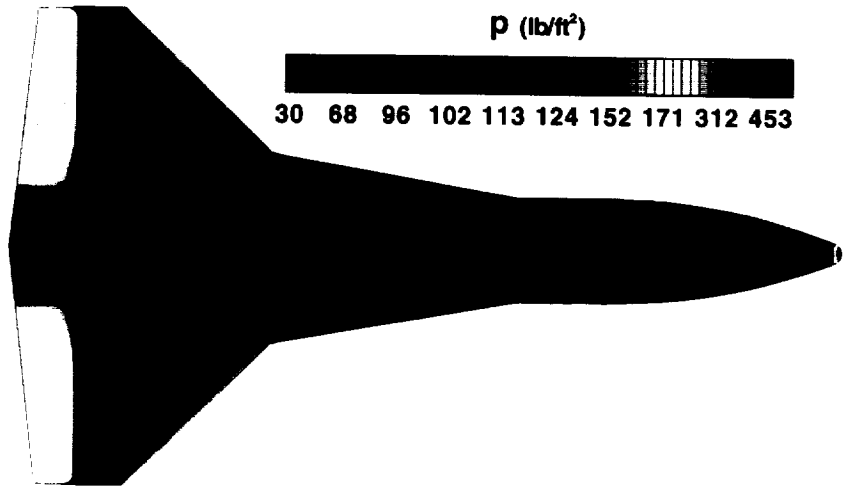

a) Wind side.

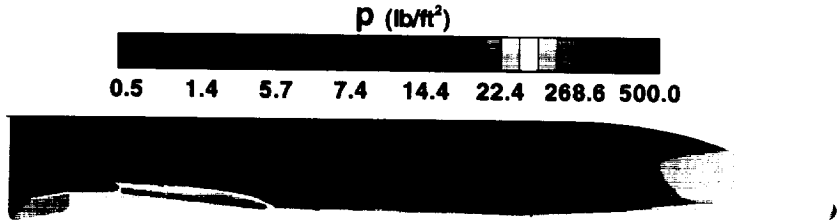

b) Starboard side.

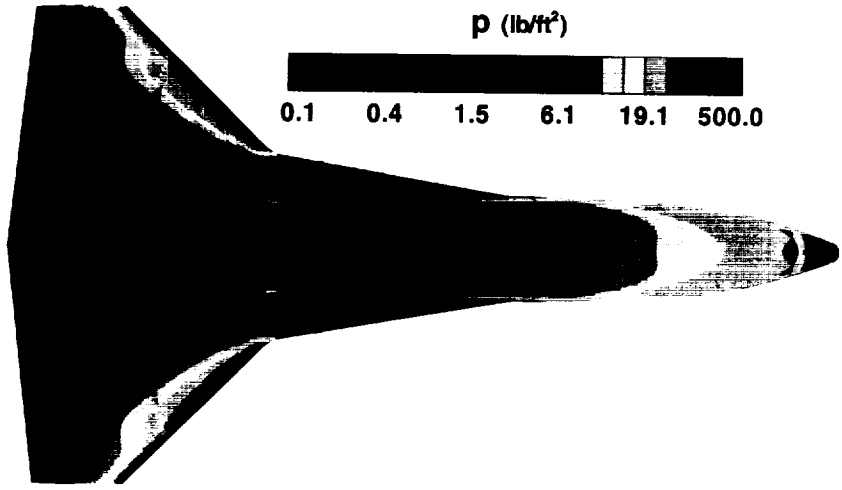

c) Lee side.

Figure 26. Pressure Distributions (Case 2b).

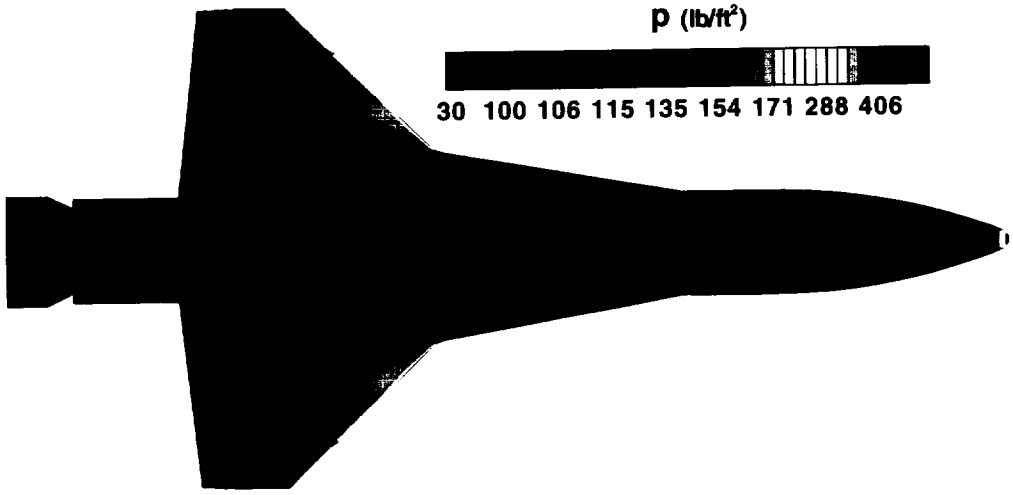

a) Wind side.

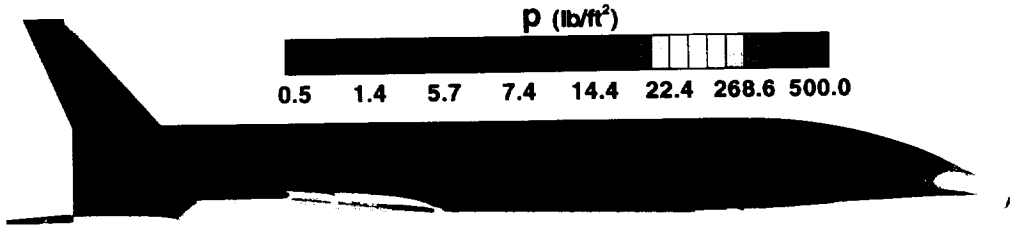

b) Starboard side.

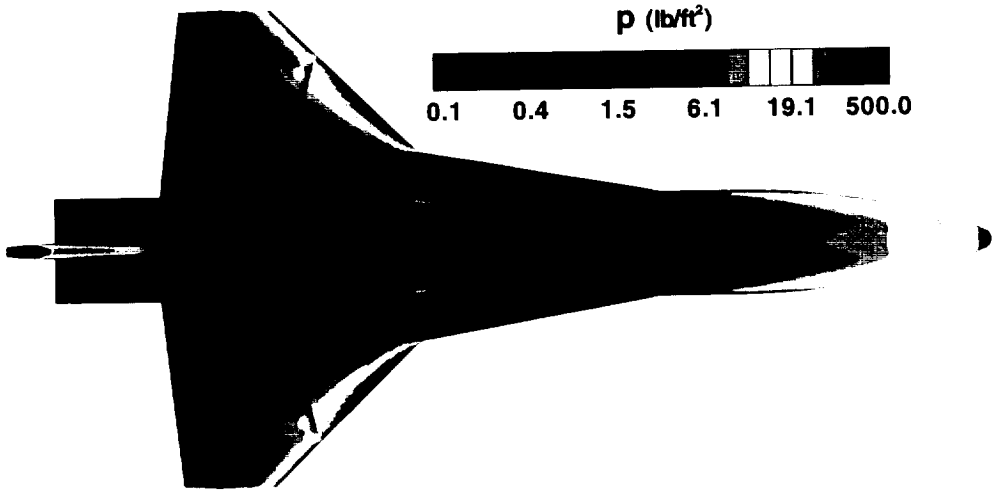

c) Lee side.

Figure 27. Pressure Distributions (Case 1a), *laminar*.

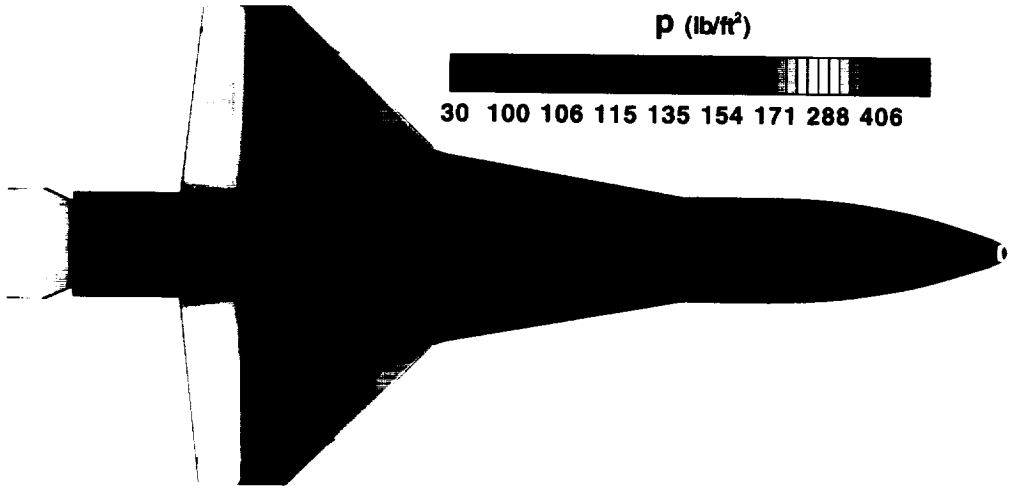

a) Wind side.

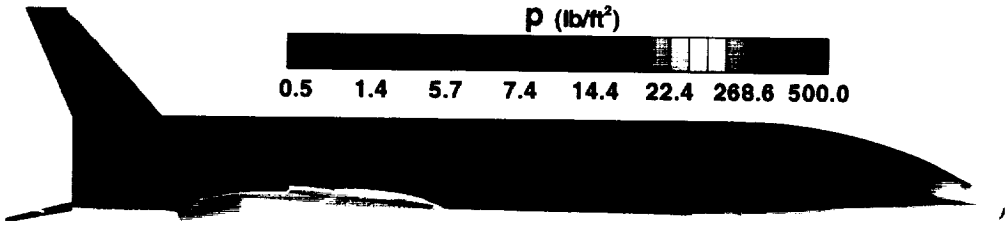

b) Starboard side.

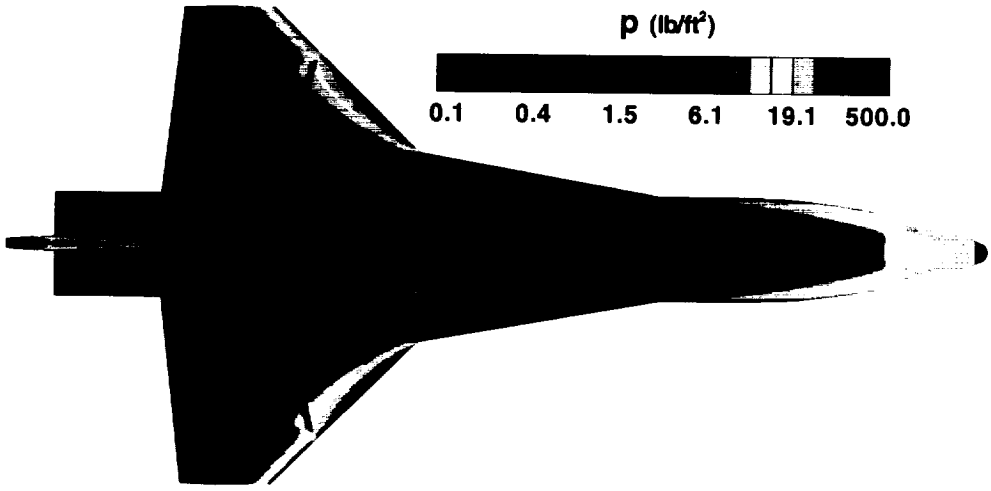

c) Lee side.

Figure 28. Pressure Distributions (Case 1b), *laminar*.

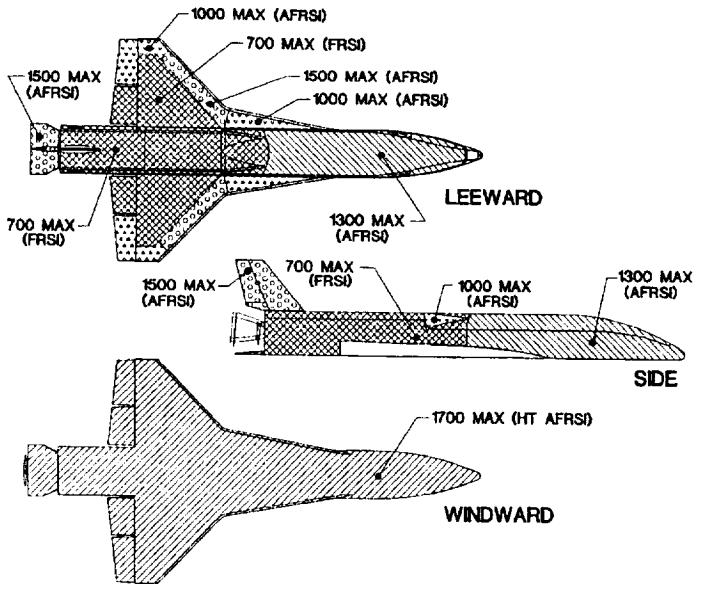

Figure 29. Thermal protection system multi-use temperature limits (°F).

TPS Considerations

As provided by OSC, the general layout of the TPS materials is given in Fig. 29, indicating the materials' respective temperature limits while the TPS blanket orientations are depicted in Fig. 30.

As a result of comparing the Case 2 temperature distributions from Figs. 13 and 14 and the TPS temperature limits shown in Fig. 29, the bond line between the AFRSI and FRSI blankets on the lee side near the wing leading edge was moved aft to account for the increased exposure found at 15 degs. angle of attack. The TPS treatment on the lee side of the nose region was also changed for this reason.

By comparing predicted near-surface streamlines of Fig. 9, the TPS material layout in Fig. 29, and the TPS blanket orientations of Fig. 30, one can investigate aspects of the TPS orientations. For example, upon carefully examining these figures, it is evident that no blanket-to-blanket or blanket-to-tile gaps are aligned with the local flow.

Concluding Remarks

Radiative equilibrium surface temperatures, heating rates, streamlines, surface pressures, and flow-field features as predicted by the LAURA code were presented for the X-34 Technology Demonstrator. Results for two trajectory points near peak heating and the effects of control surface deflections were presented for fully turbulent flow. Laminar flow results were also presented to illustrate the effects of the boundary-layer state. The effects of the results on the TPS design were also indicated. The presented results of wall temperature were used

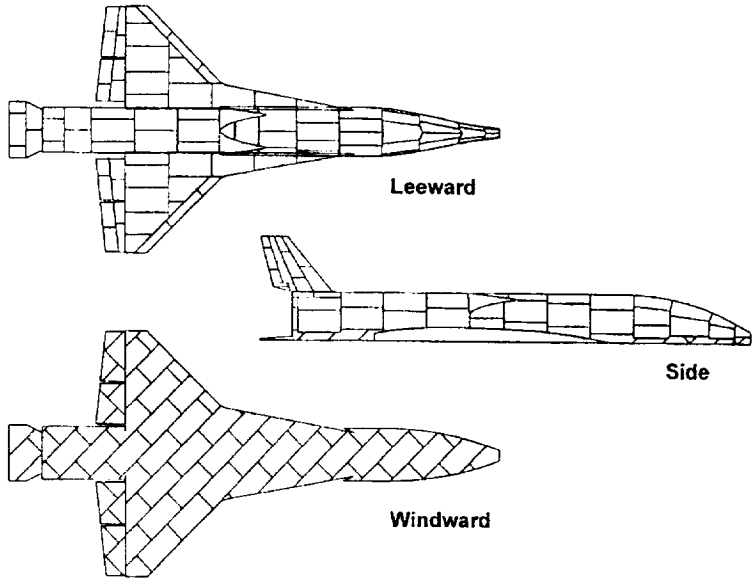

Figure 30. Thermal protection blanket layout.

extensively to ensure that the temperature limits of the selected TPS blankets will not be exceeded.

Results show that downward deflection of control surfaces substantially increases the temperatures they experience during flight. Furthermore, a "notched" body flap design creates an embedded shock which creates large heating rates on the tapered portion of the body-flap side wall.

The effect of lowering the angle of attack from 23 to 15 deg. at flight conditions was shown to substantially increase the extent of lee-side heating on the nose-canopy region and aft of the wing leading edges. Also shown was that using turbulent boundary-layer heating results is considerably more conservative than using results which model a fully laminar boundary layer.

Acknowledgments

The authors would like to thank Graphic Artist Richard Wheless of NCI Information Systems, Hampton, Virginia for generating Fig. 1, Norma Bean of Computer Sciences Corporation, Hampton, Virginia for generating the surface grid database; and Stephen Alter of Lockheed Martin Engineering & Sciences, Hampton, Virginia, for generating the volume grids essential to the results contained within.

In addition, we would like to thank Orbital Sciences Corporation of Dulles, Virginia for providing the impetus for such an exciting project.

This paper was typeset in Donald Knuth's 10pt Computer Modern using the *free*, multi-

platform TEX typesetting system and Kleb's nasa package[44] (among others).

References

[1]Elias, A. L., Hays, D., and Kennedy, J., "Pioneering Industry/Goverment Partnerships: X-34," AIAA Paper 95-3777, Sep. 1995.

[2]Anon., "X-34 to be Acid Test for Space Commerce," *Aviation Week & Space Technology*, Vol. 142, No. 14, Apr. 1995, pp. 44–53.

[3]NASA, "Reusable Launch Vehicle (RLV), Small Reusable Booter, X-34," Cooperative Agreement Notice CAN 8-2, Jan. 1995.

[4]Freeman, Jr., D. C., Talay, T. A., and Austin, R. E., "Single-Stage-to-Orbit Meeting the Challenge," *Acta Astronautica*, Vol. 38, No. 4–8, Feb.-Apr. 1996, pp. 323–331.

[5]Smith, B. A. and Asker, J. R., "NASA Speeds Selection of X-33, X-34 Plans," *Aviation Week & Space Technology*, Vol. 142, No. 11, Mar. 1995, pp. 107–109.

[6]Foley, T. M., "Big Hopes for Small Launchers," *Aerospace America*, Vol. 33, No. 7, Jul. 1995, pp. 28–34.

[7]Anon., "X-34 in Virtual Shutdown as OSC Ponders Pullout," *Aviation Week & Space Technology*, Vol. 144, No. 6, Feb. 1996, pp. 86.

[8]Anselmo, J. C., "NASA Issues Wake-Up Call to Industry," *Aviation Week & Space Technology*, Vol. 144, No. 8, Feb. 1996, pp. 20–21.

[9]NASA, "Proceedings of the X-15 First Flight 30th Anniversary Celebration," NASA CP 3105, Jun. 1991.

[10]Eisele, A., "Orbital Sciences Gets X-34 Nod Again," *Space News*, Vol. 7, No. 25, Jun. 1996, pp. 4.

[11]Anselmo, J. C., "NASA Gives Second Shot at X-34," *Aviation Week & Space Technology*, Vol. 144, No. 25, Jun. 1996, pp. 31.

[12]Riley, C. J., Kleb, W. L., and Alter, S. J., "Aeroheating Predictions for X-34 Using an Inviscid-Boundary Layer Method," AIAA Paper 98–0880, Jan. 1998.

[13]Berry, S. A., Horvath, T. J., DiFulvio, M., Glass, C. E., and Merski, N. R., "X-34 Experimental Aeroheating at Mach 6 and 10," AIAA Paper 98–0881, Jan. 1998.

[14]Wurster, K. E., Riley, C. J., and Zoby, E. V., "Engineering Aerothermal Analysis for X-34 Thermal Protection Design," AIAA Paper 98–0882, Jan. 1998.

[15]Palmer, G. and Polsky, S., "A Heating Analysis of the Nosecap and Leading Edges of the X-34 Vehicle," AIAA Paper 98–0878, Jan. 1998.

[16]Milos, F. S. and Squire, T. H., "Thermal Structural Anlaysis of SIRCA Tile for X-34 Wing Leading Edge TPS," AIAA Paper 98–0883, Jan. 1998.

[17]Carr, J. R. and Barber, D., "Blanket Design, Analysis and Testing for the X-34 Thermal Protection System," AIAA Paper 98 00884, Jan. 1998.

[18]Gnoffo, P. A., "Upwind-Biased, Point-Implicit Relaxation Strategies for Viscous, Hypersonic Flows," AIAA Paper 89 1972, 1989.

[19]Gnoffo, P. A., "An Upwind-Biased, Point-Implicit Relaxation Algorithm for Viscous, Compressible Perfect-Gas Flows," NASA TP 2953, Feb. 1990.

[20]Gnoffo, P. A., Gupta, R. N., and Shinn, J., "Conservation Equations and Physical Models for Hypersonic Air Flows in Thermal and Chemical Nonequilibrium," NASA TP 2867, 1989.

[21]Roe, P. L., "Approximate Riemann Solvers, Parameter Vectors, and Difference Schemes," *Journal of Computational Physics*, Vol. 43, Oct. 1981, pp. 357 372.

[22]Harten, A., "High Resolution Schemes for Hyperbolic Conservation Laws," *Journal of Computational Physics*, Vol. 49, No. 2, Feb. 1983, pp. 357 393.

[23]Yee, H. C., "On Symmetric and Upwind TVD Schemes," NASA TM 88325, 1986.

[24]Mitcheltree, R. A., "Computational Aerothermodynamics for Mars Pathfinder Including Turbulence," AIAA Paper 95 3493, Aug. 1995.

[25]Gnoffo, P. A., Weilmuenster, K. J., Braun, R. D., and Cruz, C. I., "Effects of Sonic Line Transition on Aerothermodynamics of the Mars Pathfinder Probe," AIAA Paper 97 1825, Jun. 1995.

[26]Mitcheltree, R. A., Moss, J. N., Cheatwood, F. M., Greene, F. A., and Braun, R. D., "Aerodynamics of the Mars Microprobe Entry Vehicles," AIAA Paper 97 3658, Aug. 1997.

[27]Mitcheltree, R. A., Wilmoth, R. G., Cheatwood, F. M., Brauckmann, G. J., and Greene, F. A., "Aerodynamics of Stardust Sample Return Capsule," AIAA Paper 97 2304, Jun. 1997.

[28]Wood, W. A., Gnoffo, P. A., and Rault, D. F. G., "Aerodynamic Analysis of Commercial Experiment Transporter Re-Entry Capsule," *Journal of Spacecraft and Rockets*, Vol. 33, No. 5, Sep. 1996, pp. 643–646.

[29]Hamilton, II, H. H., Weilmuenster, K. J., and Horvath, T. J., "Computational/Experimental Aeroheating Predictions for X-33 Phase II Vehicle," AIAA Paper 98 0869, Jan. 1998.

[30]Greene, F. A., Weilmuenster, K. J., and Micol, J. R., "Predicted Aerodynamics for a Proposed Personnel Launch Vehicle," AIAA Paper 90 1668, Jun. 1990.

[31]Kleb, W. L. and Weilmuenster, K. J., "Characteristics of the Shuttle Orbiter Leeside Flow During a Re-Entry Condition," *AIAA Journal of Spacecraft and Rockets*, Vol. 31, No. 1, Jan.-Feb. 1994, pp. 8 16, (See also AIAA Paper 92 2951.).